Available online at www.sciencedirect.com
ScienceDirect
Journal of the European Ceramic Society 31 (2011) 43–59
www.elsevier.com/locate/jeurceramsoc

Thermodynamic modeling of the NiO–SiO_2, MgO–NiO, CaO–NiO–SiO_2, MgO–NiO–SiO_2, CaO–MgO–NiO and CaO–MgO–NiO–SiO_2 systems

Dae-Hee Woo [a], Hae-Geon Lee [b], In-Ho Jung [c,*]

[a] Steelmaking Research Group, Technical Research Laboratories, POSCO, Pohang 790-785, South Korea
[b] Graduate Institute of Ferrous Technology (GIFT), Pohang University of Science and Technology (POSTECH), Pohang 790-784, South Korea
[c] Department of Mining and Materials Engineering, McGill University, H.W. Wong Building, 3610 University Street, Montreal, Quebec H3A 2B2, Canada

Received 10 March 2010; received in revised form 10 August 2010; accepted 25 August 2010

Abstract

A complete literature review, critical evaluation and thermodynamic optimization of phase equilibrium and thermodynamic properties of all available oxide phases in the NiO–SiO_2, MgO–NiO, CaO–NiO–SiO_2, MgO–NiO–SiO_2, CaO–MgO–NiO and CaO–MgO–NiO–SiO_2 systems at 1 bar pressure are presented. The molten oxide phase is described by the modified quasichemical model, and the Gibbs energies of solid olivine and pyroxene solutions were modeled using the compound energy formalism. A set of optimized model parameters of all phases is obtained which reproduces all available and reliable thermodynamic and phase equilibrium data within experimental error limits from 25 °C to above the liquidus temperatures over the entire composition range. The unexplored ternaries and quaternary phase diagrams and activity of liquid phase in the CaO–MgO–NiO–SiO_2 system have been predicted for the first time. The database of the model parameters can be used along with software for Gibbs energy minimization to calculate all thermodynamic properties and any phase diagram section of interest.

Keywords: Thermodynamic modeling; Thermal properties; Silicate

1. Introduction

Thermodynamic behaviour of NiO in the CaO–FeO–Fe_2O_3–MgO–SiO_2 slag is important in the pyrometallurgical ferro-nickel production process.[1,2] In geochemistry, the partition of Ni oxide between Mg-rich olivine and molten oxide can provide valuable information to understand the thermo-chemistry of upper mantle and meteorites formation.[3,4] However, the phase diagrams and thermodynamic properties of the CaO–FeO–Fe_2O_3–MgO–NiO–SiO_2 system have been poorly investigated.

The main goal of the present study is to perform a complete review, critical evaluation and optimization of thermodynamic properties at 1 bar total pressure of all oxide phases in the NiO–SiO_2, MgO–NiO, CaO–NiO–SiO_2, MgO–NiO–SiO_2, CaO–MgO–NiO and CaO–MgO–NiO–SiO_2 systems. In the thermodynamic "optimization" of a chemical system, all available thermodynamic and phase equilibrium data are evaluated simultaneously in order to obtain one set of model equations for the Gibbs energies of all phases as functions of temperature and composition. From these equations, all of the thermodynamic properties and the phase diagrams can be back-calculated. In this way, all the data are rendered self-consistent and consistent with thermodynamic principles. Thermodynamic property data, such as activity data, can aid in the evaluation of the phase diagram, and phase diagram measurements can be used to deduce thermodynamic properties. Discrepancies in the available data can often be resolved, and interpolations and extrapolations can be made in a thermodynamically correct manner. The resultant model database provides the best presently available description of the thermodynamic properties and phase equilibria.

The present thermodynamic modeling of the CaO–MgO–NiO–SiO_2 system is part of a research program aimed at complete characterization of phase equilibria and thermodynamic properties of the FeO–Fe_2O_3–CaO–MgO–SiO_2–NiO–CoO system[5–9] which has various applications in the pyrometallurgical Fe–Ni and Fe–Co productions, geochemistry, and so on.

* Corresponding author. Tel.: +1 514 398 2608; fax: +1 514 398 4492.
E-mail address: in-ho.jung@mcgill.ca (I.-H. Jung).

0955-2219/$ – see front matter © 2010 Elsevier Ltd. All rights reserved.
doi:10.1016/j.jeurceramsoc.2010.08.019

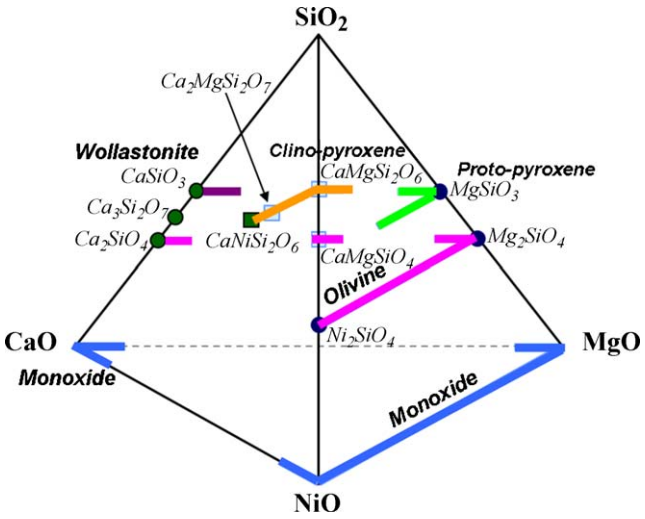

Fig. 1. Schematic representation of the CaO–MgO–NiO–SiO_2 system.

2. Phases and thermodynamic models

The following solution and stoichiometric phases are found in the CaO–MgO–NiO–SiO_2 system (see Fig. 1):

(i) Slag (molten oxide phase): CaO–MgO–NiO–SiO_2. Liquid miscibility gap can be found in SiO_2-rich region.
(ii) *Olivine*: $(Ca^{2+}, Mg^{2+}, Ni^{2+})^{M2}[Ca^{2+}, Mg^{2+}, Ni^{2+}]^{M1}SiO_4$. A complete solution between Mg_2SiO_4 (forsterite) and Ni_2SiO_4 exists. There are no mutual solubility between Ni_2SiO_4 and Ca_2SiO_4 and a limited solubility between Ca_2SiO_4 and Mg_2SiO_4. $CaMgSiO_4$ (monticellite) is also part of the olivine solution.
(iii) *Proto-pyroxene*: $(Ca^{2+}, Mg^{2+}, Ni^{2+})^{M2}[Mg^{2+}, Ni^{2+}]^{M1}Si_2O_6$. This is a $MgSiO_3$ (enstatite) based solution with limited solubilities of $NiSiO_3$ and $CaMgSi_2O_6$.
(iv) *Clino-pyroxene*: $(Ca^{2+}, Mg^{2+}, Ni^{2+})^{M2}[Mg^{2+}, Ni^{2+}]^{M1}Si_2O_6$. This is a complete solid solution between $CaMgSiO_6$ (diopside) and $CaNiSiO_6$ (niopside) with a limited solubility of $MgSiO_3$.
(v) *Monoxide*: $(Ca^{2+}, Mg^{2+}, Ni^{2+})O$. This is a complete solution between MgO and NiO with a limited solubility of CaO. CaO can dissolve limited amounts of NiO and MgO.
(vi) *Other solutions*: α-Ca_2SiO_4, α′-Ca_2SiO_4 and $CaSiO_3$ (wollastonite) solutions.
(vii) *Stoichiometric compounds*: $CaSiO_3$ (pseudowollastonite), Ca_3SiO_5 (hatrurite), $Ca_3Si_2O_7$ (rankinite), $Ca_2MgSi_2O_7$ (akermanite), $Ca_3MgSi_2O_8$ (merwinite) and SiO_2.

Cations shown within a set of brackets for olivine and pyroxenes occupy the same sublattice.

2.1. Molten oxide (slag)

For the molten oxide (slag) phase, the modified quasichemical model,[10,11] which takes into account the second-nearest-neighbour (SNN) short-range-ordering (SRO) of molten oxide, was used. For example, the SNN exchange reactions for the CaO–NiO–SiO_2 slag are:

$$(\text{Ni–Ni}) + (\text{Si–Si}) = 2(\text{Ni–Si}), \qquad \Delta g_{\text{NiSi}} \tag{1}$$

$$(\text{Ca–Ca}) + (\text{Si–Si}) = 2(\text{Ca–Si}), \qquad \Delta g_{\text{CaSi}} \tag{2}$$

$$(\text{Ca–Ca}) + (\text{Ni–Ni}) = 2(\text{Ca–Ni}), \qquad \Delta g_{\text{CaNi}} \tag{3}$$

where $(m–n)$ represents a second-nearest-neighbour $m–n$ pair. The Gibbs energy of the liquid solution is given by:

$$G = (n_{\text{NiO}} g^{o}_{\text{NiO}} + n_{\text{CaO}} g^{o}_{\text{CaO}} + n_{\text{SiO}_2} g^{o}_{\text{SiO}_2}) - T\,\Delta S^{\text{config}} + n_{\text{NiSi}}\left(\frac{\Delta g_{\text{NiSi}}}{2}\right) + n_{\text{CaSi}}\left(\frac{\Delta g_{\text{CaSi}}}{2}\right) + n_{\text{NiCa}}\left(\frac{\Delta g_{\text{NiCa}}}{2}\right) \tag{4}$$

where n_{NiO}, n_{CaO} and n_{SiO_2} are the numbers of moles of the components in solution, and the n_{mn} are the numbers of second-nearest-neighbour $(m–n)$ bonds at equilibrium. ΔS^{config} is the configurational entropy of mixing expression for the random mixing of the bonds over "bond sites" in the Ising approximation, and is a function of the n_{mn}. The full expression can be found in the previous studies.[10,11] The numbers of bonds, n_{mn}, at equilibrium are given by minimizing G with respect to the n_{mn} at constant overall composition: $\partial G/\partial n_{mn} = 0$.

This results effectively in "equilibrium constants" for the quasichemical reactions (1)–(3). For example, since Δg_{NiSi} is negative, the equilibrium in reaction (1) is shifted to the right, and (Ni–Si) bonds predominate over (Ni–Ni) and (Si–Si) bonds. Second-nearest-neighbour coordination numbers, Z_{mm} and Z_{nn}, are also introduced as described previously.[10,11] Compositions are expressed in terms of "coordination equivalent mole fractions", Y_m, of the components. These are the mole fractions weighted by the coordination numbers.

The binary model parameters Δg_{mn} are expanded as empirical polynomials in the composition variables Y_m, and the parameters are obtained by optimization of the binary thermodynamic and phase diagram data:

$$\Delta g_{mn} = \sum_{i,j} q^{ij}_{mn} Y^{i}_{m} Y^{j}_{n} \tag{5}$$

Once the three binary sub-systems of a ternary system have been optimized, the properties of the ternary liquid solution can be estimated from the binary parameters using the ternary interpolation technique as described previously.[20,21] The Gibbs energies of the ternary liquid CaO–NiO–SiO_2 and MgO–NiO–SiO_2 solutions were calculated using the asymmetric 'Toop-like'[20,21] interpolation technique from the binary model parameters with SiO_2 as the "asymmetric component". In the case of the ternary CaO–MgO–NiO system, the 'Kohler-like' interpolation technique was used.

In order to reproduce the ternary phase diagrams and thermodynamic data more accurately, small optimized ternary model parameters were introduced for CaO–NiO–SiO_2 and MgO–NiO–SiO_2 system. For instance, for the CaO–NiO–SiO_2 system, an empirical ternary term $q^{001}_{\text{CaSi(Ni)}} Y_{\text{CaO}} Y_{\text{SiO}_2} Y^{1}_{\text{NiO}}$ was

included in the expression for Δg_{CaSi}, where $q^{001}_{CaSi(Ni)}$ is a parameter obtained by optimization of the ternary data. This term describes the influence of the presence of Ni on the formation energy Δg_{CaSi} of reaction (3). Note that this term is equal to zero in the CaO–SiO_2 binary system where $Y_{NiO} = 0$.

Then, the thermodynamic properties of the quaternary CaO–MgO–NiO–SiO_2 liquid were predicted from those of four ternary sub-systems. This model has successfully been applied to the thermodynamic description of multicomponent molten oxide solutions.[5–9,12–19]

2.2. Olivine

The olivine solid solution has two distinct octahedral sublattices, called M2 and M1 site[22–24]:

$$(Ca^{2+}, Mg^{2+}, Ni^{2+})^{M2}[Ca^{2+}, Mg^{2+}, Ni^{2+}]^{M1}SiO_4 \quad (6)$$

where cations shown within a set of brackets occupy the same sublattice.

Because the M2 site is bigger than M1 site, cations with large size preferentially enter the M2 sites. The size of cations are in the order of $Ca^{2+} > Mg^{2+} > Ni^{2+}$.[25] In the present study, the olivine model is developed within the framework of the compound energy formalism (CEF).[26] The Gibbs energy expression in the CEF per formula unit of a solution is as follows:

$$G = \sum_i \sum_j Y_i^{M2} Y_j^{M1} G^o_{ij} - TS_C + G^E \quad (7)$$

where Y_i^{M2} and Y_j^{M1} represent the site fractions of constituents i and j on the M2 and M1 sublattices, G^o_{ij} is the Gibbs energy of an "end-member" $(i)^{M2}[j]^{M1}SiO_4$, in which the M2 and M1 sublattices are occupied only by i and j cations respectively, S_C is the configurational entropy assuming random mixing on each sublattice given by:

$$S_C = -R\left(\sum_i Y_i^{M2} \ln Y_i^{M2} + \sum_j Y_j^{M1} \ln Y_j^{M1}\right) \quad (8)$$

and G^E is the excess Gibbs energy given by:

$$G^E = \sum_i \sum_j \sum_k Y_i^{M2} Y_j^{M2} Y_k^{M1} L_{ij:k} + \sum_i \sum_j \sum_k Y_k^{M2} Y_i^{M1} Y_j^{M1} L_{k:ij} \quad (9)$$

where $L_{ij:k}$ and $L_{k:ij}$ are interaction energies between cations i and j on one sublattice when the other sublattice is occupied by k. The dependence of the interaction energies on composition can be expressed by Redlich–Kister power series:

$$L_{ij:k} = \sum_m {}^m L_{ij:k} (Y_j^{M2} - Y_i^{M2})^m \quad (10)$$

$$L_{k:ij} = \sum_m {}^m L_{k:ij} (Y_j^{M1} - Y_i^{M1})^m \quad (11)$$

For the present olivine solution, there are nine end-members. Among them, the Gibbs energies of four end-members Ca_2SiO_4, Mg_2SiO_4, $CaMgSiO_4$ and $MgCaSiO_4$ were already determined in the previous study.[5] The Gibbs energy of Ni_2SiO_4 is determined in the present study, based on thermodynamic data in NiO–SiO_2 system. In order to determine the Gibbs energies of $CaNiSiO_4$, $NiCaSiO_4$, $MgNiSiO_4$ and $NiMgSiO_4$ end-members, two physically meaningful model parameters like I (for inverse reaction) and Δ (for reciprocal reaction) were used in the present study instead of specifying the Gibbs energy independently:

$$I_{AB} = G^o_{AB} - G^o_{BA} \quad (12)$$

$$\Delta_{AB:BA} = G^o_{AA} + G^o_{BB} - G^o_{AB} - G^o_{BA} \quad (13)$$

The I_{AB} has the physical significance of being equal to the energy change of the reaction when A^{2+} and B^{2+}, occupying M2 and M1 sites respectively, change places: $(A^{2+})^{M2} + [B^{2+}]^{M1} = [A^{2+}]^{M1} + (B^{2+})^{M2}$. Similarly, the $\Delta_{AB:BA}$ has physical significance as the energy change of the reciprocal exchange reaction among end-members.

2.3. Pyroxenes

There are four kinds of pyroxene solutions with crystal structures, P*bcn* (proto-pyroxene), C*2/c* (clino-), P*bca* (ortho-) and P*21/c* (low clino-). For the NiO containing systems, the thermodynamic behaviours for the proto- and clino-pyroxenes have been investigated. Like olivine, the pyroxenes have two distinct octahedral sublattices, M2 and M1.[22–24] However, unlike olivine, the amount of Ca^{2+} on the M1 sites is negligibly small, so that the formula unit of pyroxenes can be written as:

$$(Ca^{2+}, Mg^{2+}, Ni^{2+})^{M2}[Mg^{2+}, Ni^{2+}]^{M1}Si_2O_6 \quad (14)$$

The Gibbs energy of a pyroxene solution is expressed using the compound energy formalism[26] in Eq. (7). Among six end-member Gibbs energies, two Gibbs energies for the $CaMgSi_2O_6$, $MgMgSi_2O_6$ were determined in the previous study.[5] Like olivine solution, the Gibbs energies of all other end-members were determined based on the available thermodynamic and phase equilibrium data.

2.4. Monoxide

CaO and MgO have limited solubilities in each other forming a solid miscibility gap. The same happens for the CaO–NiO system. On the other hand, a complete monoxide solid solution exists between MgO and NiO.

A simple random mixing model with a polynomial expansion of the excess Gibbs energy is used for the monoxide solution:

$$G = (G^o_A X_A + G^o_B X_B) + nRT(X_A \ln X_A + X_B \ln X_B) + G^E \quad (15)$$

$$G^E = \sum q^{ij}_{AB} (X_A)^i (X_B)^j \quad (16)$$

In the case of the monoxide solution, $n = 1$ because one mole of cations such as Ca, Mg and Ni are mixing for one mole of the monoxide solution. The previously optimized model parameters for the CaO–NiO[27] and CaO–MgO[28] solutions were used without any modification and the MgO–NiO solution was newly optimized in the present study. Thermodynamic properties of

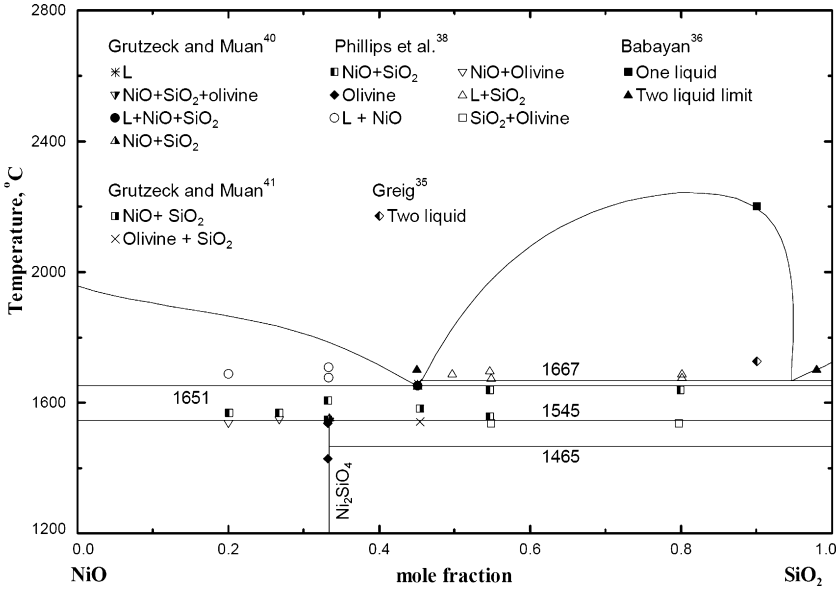

Fig. 2. Calculated phase diagram of the NiO–SiO_2 system along with experimental data.[35,36,38,40,41]

the ternary CaO–MgO–NiO monoxide solution were predicted using the 'Kohler-like'[20,21] interpolation technique.

2.5. Other solid solutions

The previous thermodynamic model and optimized parameters[5] for wollastonite, α-Ca_2SiO_4 and α′-Ca_2SiO_4 solid solutions are taken without any modification. These solutions are described with the random mixing model, as described in Eq. (15), in the consideration of simple replacement of Ca^{2+} by Mg^{2+}: (Ca^{2+}, Mg^{2+})SiO_3 and (Ca^{2+}, Mg^{2+})$_2SiO_4$.

2.6. Stoichiometric compounds

$CaSiO_3$ (pseudowollastonite), Ca_3SiO_5 (hatrurite), $Ca_3Si_2O_7$ (rankinite), $Ca_2MgSi_2O_7$ (akermanite), $Ca_3MgSi_2O_8$ (merwinite) and SiO_2 are considered to be stoichiometric compounds in this study. The Gibbs energies of the compounds can be found in the previous studies.[29–31]

3. Critical evaluation/optimization

All literature data related to the thermodynamic properties, phase equilibria and phase diagrams for the CaO–MgO–NiO–SiO_2 system were collected and critically evaluated to obtain one set of model parameters to reproduce all the reliable experimental data within experimental error limits. All the calculations in the present study were carried out using the FactSage[29] thermochemical software.

3.1. CaO–SiO_2 CaO–MgO, CaO–NiO and MgO–SiO_2 systems

Four binary systems, the CaO–SiO_2[32], CaO–MgO[28], CaO–NiO[27] and MgO–SiO_2[33] systems, were previously optimized. The monoxide solutions in the CaO–NiO and CaO–MgO systems have miscibility gaps. In the case of the CaO–SiO_2 and MgO–SiO_2 systems, liquid miscibility gaps can be found at high SiO_2 region. The previously optimized model parameters were adopted in the present study without any modification.

3.2. NiO–SiO_2 system

Alejandro Cruz et al.[34] performed the thermodynamic modeling of the NiO–SiO_2 system using the structural model for liquid phase. However, the critical review of all literature data was not presented in their study. Thus, it is worthwhile to do critical review of the NiO–SiO_2 system.

Fig. 2 shows the optimized phase diagram of the NiO–SiO_2 system in the present study. Greig[35] investigated the liquid miscibility gap in silica-rich melts at near 1700 °C using a classical quenching technique with an optical microscopic phase determination. Babayan[36] investigated the miscibility gap using the same technique. In particular, he reported that the miscibility gap at $X_{SiO_2} = 0.9$ disappeared above 2200 °C. Ni_2SiO_4 (olivine) is the only intermediate compound observed in this system. Ringwood[37] reported the incongruent melting behaviour of Ni_2SiO_4 to NiO and liquid at 1625 ± 20 °C using a classical quenching technique with optical microscopic observation. Phillips et al.[38] reinvestigated the phase diagram of the NiO–SiO_2 system using the same technique and found that Ni_2SiO_4 decomposed to NiO and SiO_2 (cristobalite) at 1545 ± 5 °C before melting. Later, O'Neill[39] and Grutzeck and Muan[40,41] also confirmed the decomposition of Ni_2SiO_4 at 1547 ± 5 °C using the X-ray diffraction (XRD) analysis. The calculated diagram can well reproduce the experimental data except for the monotectic reaction. The calculated monotectic reaction at 1667 °C is slightly lower than reported temperature 1685 ± 10 °C by Philip et al.[38]

The heat capacity of Ni_2SiO_4 was determined by Watanabe[42] from 350 to 750 K using a differential scanning calorimeter (DSC) and later by Robie et al.[43] from 5 to 1000 K using an adiabatic calorimeter (5–387 K) and DSC (360–1000 K).

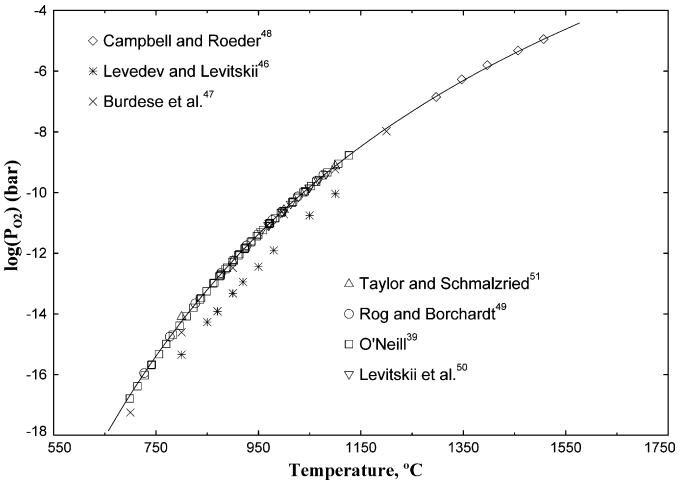

Fig. 3. Calculated equilibrium oxygen partial pressures for $Ni_2SiO_4 + SiO_2 + Ni$ assemblage along with experimental data.[39,46–51]

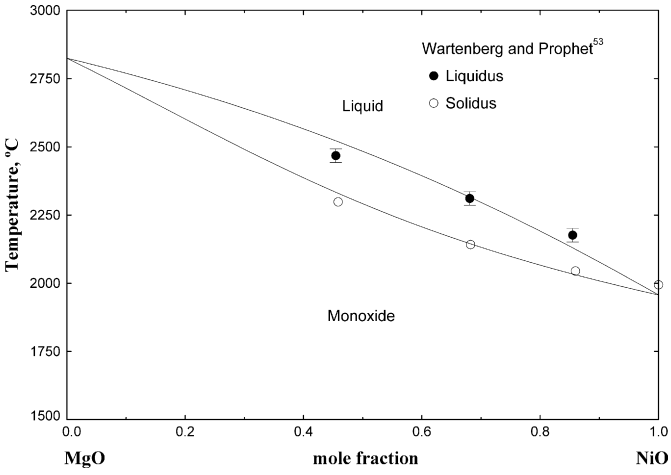

Fig. 4. Calculated phase diagram of the MgO–NiO system along with experimental data of Wartenberg and Prophet.[53]

Robie et al.[43] calculated $S_{298\,K}$ from their low temperature heat capacity data as 128.1 ± 0.2 J/(mol-K), which was 4.6% smaller than the value reported by Watanabe.[42] Navrotsky[44] and Sugawara[45] measured the heat contents of Ni_2SiO_4 using a drop calorimetry technique. The measured $H_{986\,K} - H_{297\,K}$ of Ni_2SiO_4 by Navrotsky[44] was 108 ± 2 kJ/mol. Sugawara[45] measured $H_{1773\,K} - H_{298\,K}$ of Ni_2SiO_4 to be 309 ± 22 kJ/mol in Ar atmosphere and 272 ± 11 kJ/mol in air. He speculated the Ni loss would be more significant under Ar atmosphere without any experimental confirmation and explained that the difference resulted from Ni absorption into Pt capsule of drop calorimeter. However, the heat contents of NiO measured by Sugawara at 1500 °C largely deviated from the well-accepted values of Barin, 83.2 kJ/mol, by 6% in air and by 17% under Ar gas. This result indicates that the experimental data of Sugawara[45] for Ni_2SiO_4 may be erroneous.

The equilibrium oxygen partial pressures for the $Ni_2SiO_4 + SiO_2 + Ni$ assemblage were well determined over a wide temperature range between 700 and 1550 °C using a gas equilibration technique[46–48] or EMF measurement[39,49–51], which can essentially determine the Gibbs energy of Ni_2SiO_4. All these thermodynamic experimental data were used to determine the $\Delta H^o_{298\,K}$, $S^o_{298\,K}$ and C_P of the solid Ni_2SiO_4.

Fig. 3 shows the calculated equilibrium oxygen partial pressures for the $Ni_2SiO_4 + SiO_2 + Ni$ assemblage along with experimental results.[39,46–51] In the present study, $S^o_{298\,K}$ reported by Robie et al.[43] and the heat capacity function of Hirschmann[52] obtained by fitting the results of Robie et al.[43] were used without any further modification. Then, $\Delta H^o_{298\,K}$ was optimized to reproduce the experimental data in Fig. 3. The calculated oxygen partial pressures are in good agreement with the experimental data. In the present study, the $H_T - H_{298\,K}$ of Ni_2SiO_4 are calculated to be 110.4 kJ/mol at 713 °C and 255.5 kJ/mol at 1500 °C compared to the experimental data: 108 ± 2 kJ/mol of Navrotsky[44] at 713 °C and 272 ± 11 kJ/mol in air of Sugawara[45] at 1500 °C. The present calculations are in good agreement with the result of Navrotsky[44] and in a fair agreement with the results of Sugawara[45] in consideration of his experimental error.

3.3. MgO–NiO system

Wartenberg and Prophet[53] revealed that MgO and NiO are completely miscible each other in both solid and liquid states. They reported solidus and liquidus of the MgO–NiO monoxide solution using a high temperature heating microscope with a pyrometer. Fig. 4 shows the optimized phase diagram of the MgO–NiO system in the present study.

Thermodynamic properties of solid MgO–NiO monoxide solution have been determined using a calorimetry,[54,57] gas equilibration,[58–60] or EMF technique.[55,61–66] However, a considerable inconsistency is found between the experimental results. Nussler and Kubaschewski[54] measured the enthalpy of mixing using an adiabatic calorimeter and concluded the ideal behaviour of solid MgO–NiO solution. On the other hand, Davies and Navrotsky[57] observed a negative deviation from ideality using a $2PbO{\cdot}B_2O_3$ solution calorimetry as shown in Fig. 5(a). The activities of NiO measured from gas equilibration and EMF technique are summarized in Fig. 5(b). Temperature dependency of NiO activity was insignificant in most of the investigations[55,58–64,66] except Shirane[65]. Seetharaman and Abraham[61] reported a strong positive deviation from ideal behaviour, whereas the others reported ideal or negative behaviour for the solid MgO–NiO solution. The experimental data of Shirane[65] are much negative than the other experimental data due to the unknown reason. The observed deviation was also asymmetric rather than symmetric.[57,62,64,65] Davies and Navrotsky[57] explained this asymmetric deviation due to a short-range ordering supported by structural[67] and spectroscopic[68] data.

Since there are quite scatters among the experimental data for solid MgO–NiO monoxide solution, the phase equilibrium data between MgO–NiO solution and Mg_2SiO_4–Ni_2SiO_4 olivine solution in ternary MgO–NiO–SiO_2 system, which will be discussed in Section 3.5, were simultaneously considered to optimize the model parameters of the MgO–NiO monoxide solution. Clearly, the ternary experimental data could not be reproduced with positive model parameters of the monoxide solution. The parameters reproducing the results of Davies and

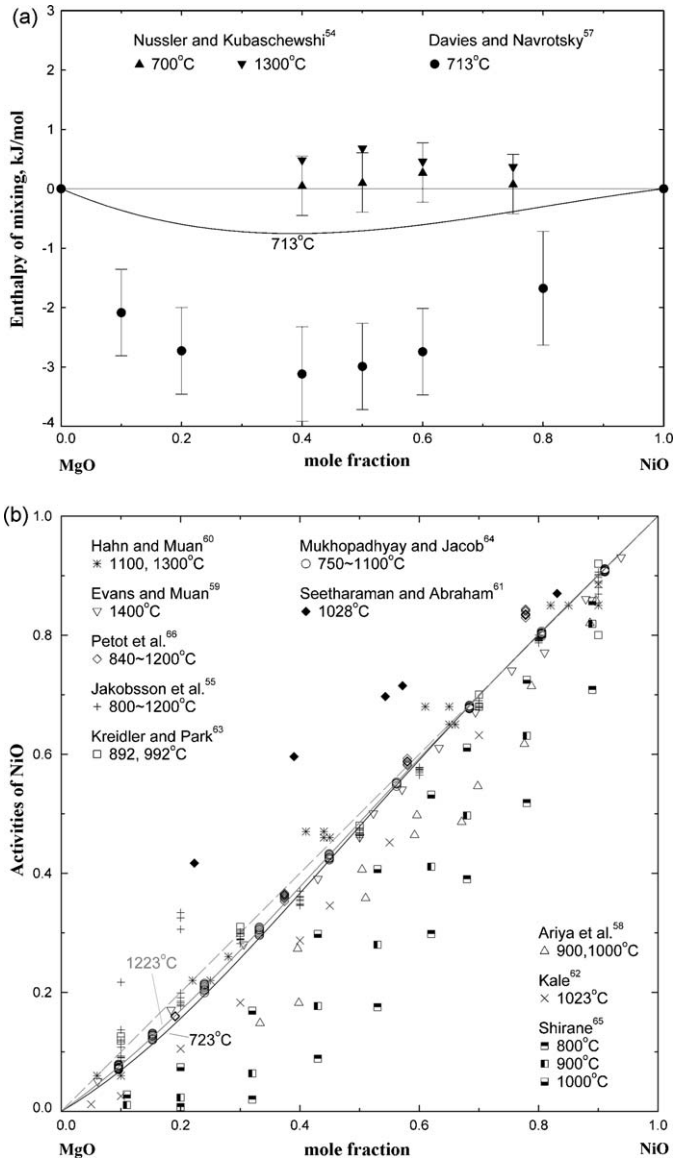

Fig. 5. Thermodynamic properties of solid MgO–NiO monoxide phase: (a) calculated enthalpy of mixing of the MgO–NiO monoxide at 713 °C along with experimental data[54,57] and (b) calculated activities of NiO (relative to solid NiO standard state) in the MgO–NiO monoxide at 723 and 1223 °C along with experimental data.[55,58–66]

Navrotsky[57] were too negative to reproduce the ternary equilibration data. The optimized model parameters of the MgO–NiO monoxide solution can reproduce the results of Mukhopadhyay and Jacob.[64]

Previously, Nussler and Kubaschewski[54] described the MgO–NiO system with the Gibbs energy of liquid deviated slightly positively from an ideal solution. On the other hand, Jakobsson et al.[55] and Zinkevich et al.[56] considered the liquid phase as an ideal solution due to insufficient thermodynamic data. In the present study, however, a slightly negative deviation of liquid solution from an ideal solution was needed to reproduce the phase diagram by Wartenberg and Prophet,[53] after the optimization of solid MgO–NiO monoxide solution.

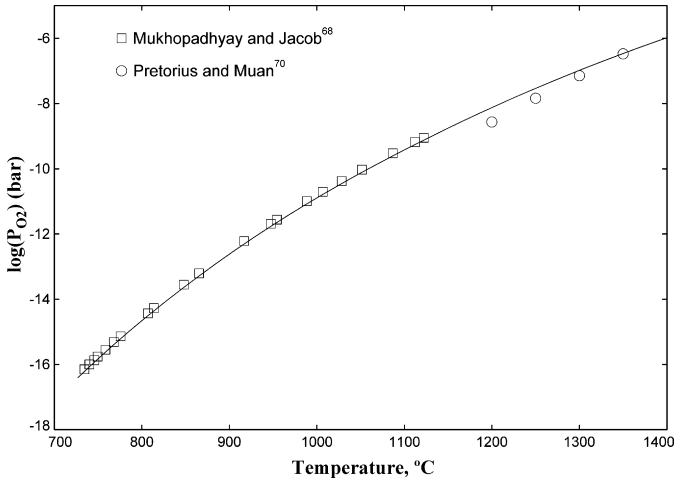

Fig. 6. Calculated equilibrium oxygen partial pressures for the $CaNiSi_2O_6 + CaSiO_3 + SiO_2 + Ni$ assemblage along with experimental data.[68,70]

3.4. *CaO–NiO–SiO₂ system*

$CaNiSi_2O_6$ (niopside) is the only ternary solid phase reported in this system. Bigger[69] and Pretorius and Muan[70] found no solubility of Ni_2SiO_4 into α- and α′-Ca_2SiO_4 phases. Gjessing[71] synthesized $CaNiSi_2O_6$ (niopside) of a clino-pyroxene structure (space group *C*2/*c*), which was also observed in the phase diagram study by Bigger[69]. No direct experimental data have been reported for the non-stoichiometry of $CaNiSi_2O_6$ phase. Pretorius and Muan[70] determined the oxygen partial pressures in equilibrium with $CaNiSi_2O_6 + CaSiO_3 + SiO_2 + Ni$ using the mixture gases of H_2 and CO_2 in the temperature range of 1200–1350 °C. Later, Mukhopadhyay and Jacob[72] measured the same equilibrium oxygen pressures using the an YSZ (Y_2O_3 stabilized ZrO_2) galvanic cell from 750 to 1150 °C. Navrotsky and Coons[73] measured the enthalpy of formation of niopside from the pure oxides to be -113.4 ± 2.1 kJ/mol at 713 °C using a $2PbO{\cdot}B_2O_3$ solution calorimetry.

No studies have been performed for $\Delta H^o_{298\,K}$, $S^o_{298\,K}$ and heat capacity for $CaNiSi_2O_6$. The heat capacity was estimated from pure oxides using the Neumann–Kopps rule. Then $\Delta H^o_{298\,K}$ and $S^o_{298\,K}$ were determined to reproduce the experimental oxygen partial pressures in Fig. 6. As can be seen in the figure, the slope of the oxygen partial pressure by Pretorius and Muan[70] is steeper than that of Mukhopadhyay and Jacob[72]. As the oxygen partial pressures can be accurately determined by a solid oxygen cell, the thermodynamic properties of $CaNiSi_2O_8$ were optimized based on the experimental data from Mukhopadhyay and Jacob[72]. The calculated formation enthalpy ($\Delta H^f_{986\,K}$) from this study is −105 kJ/mol, which is slightly higher but still in reasonable agreement with -113.4 ± 2.1 kJ/mol by Navrotsky and Coons[73]. If the experimental data of Pretorius and Muan[70] were fitted, the $\Delta H^f_{986\,K}$ would be calculated to be −171.6 kJ/mol, which is completely away from the experimental data of Navrotsky and Coons[73]. The optimized $\Delta S^o_{298\,K}$ of $CaNiSi_2O_6$ from pure oxides is −8.2 J/(mol-K).

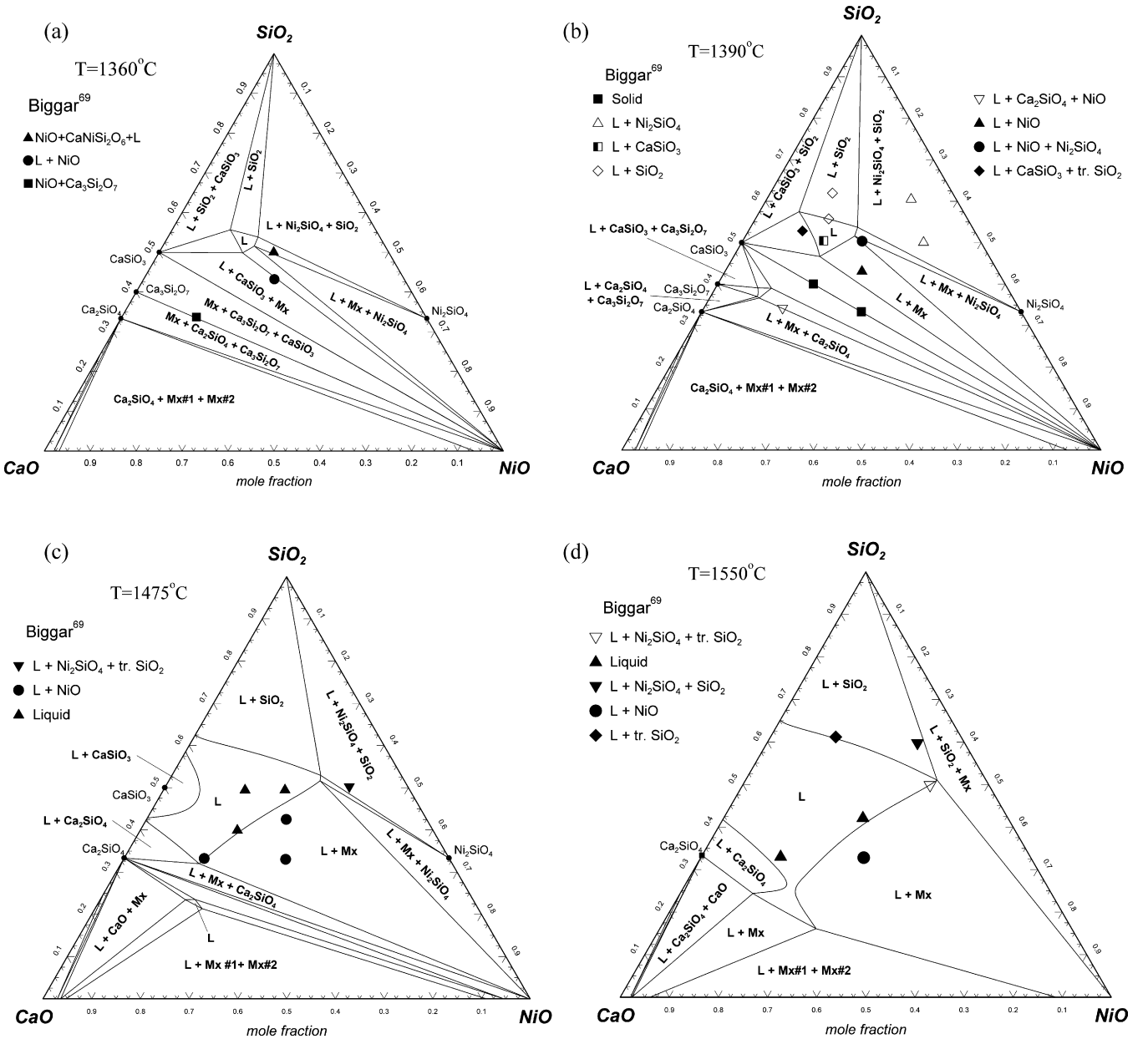

Fig. 7. Calculated phase diagrams of the NiO–CaO–SiO_2 system along with experimental data of Biggar[69] at (a) 1360 °C, (b) 1390 °C, (c) 1475 °C, and (d) 1550 °C. Mx and L represent monoxide solid solution and liquid, respectively. "tr." is the abbreviation of trace amounts.

Bigger[69] investigated the phase relation of the CaO–NiO–SiO_2 system using a classical quenching technique with the optical microscopic and X-ray diffraction phase analyses. The reported phase relations at 1360–1550 °C are well reproduced with two additional ternary model parameters for liquid phase as shown in Fig. 7. Although Bigger[69] mentioned possible solubility of Ca in Ni_2SiO_4 at 1550 °C in order to explain the presence of Ni_2SiO_4 slightly above its decomposition temperature (1545 °C), it was not experimentally confirmed and might be caused by the uncertainty of temperatures. No solubility of Ca in Ni_2SiO_4 was considered in the present study.

Pretorius and Muan[70] determined the solidus temperatures of the several solid mixtures containing 60 mol% niopside and 20 mol% of two other solid phases (see Table 1). They increased the temperature of the prepared solid mixtures and identified the

Table 1
Temperatures of the invariant equilibria measured by Pretorius and Muan[70] in the CaO–NiO–SiO_2 system: A = $CaNi_2SiO_4$, B = $CaSiO_3$ or Ni_2SiO_4, and C = SiO_2 or NiO.

Invariant equilibrum (initial amount: 0.6A + 0.2B + 0.2C)	Measured temp. (°C)	Calculated temp. (°C)
$CaNiSi_2O_6 + CaSiO_3 + SiO_2$ + liq	1338	1347
$CaNiSi_2O_6 + Ni_2SiO_4 + SiO_2$ + liq	1380	1357
$CaNiSi_2O_6 + Ni_2SiO_4$ + NiO + liq	1375	1358
$CaNiSi_2O_6 + CaSiO_3$ + NiO + liq	1348	1353
Solidus at the composition of $NiCaSi_2O_6$	1338	1347
Liquidus at the composition of $NiCaSi_2O_6$	1420	1426

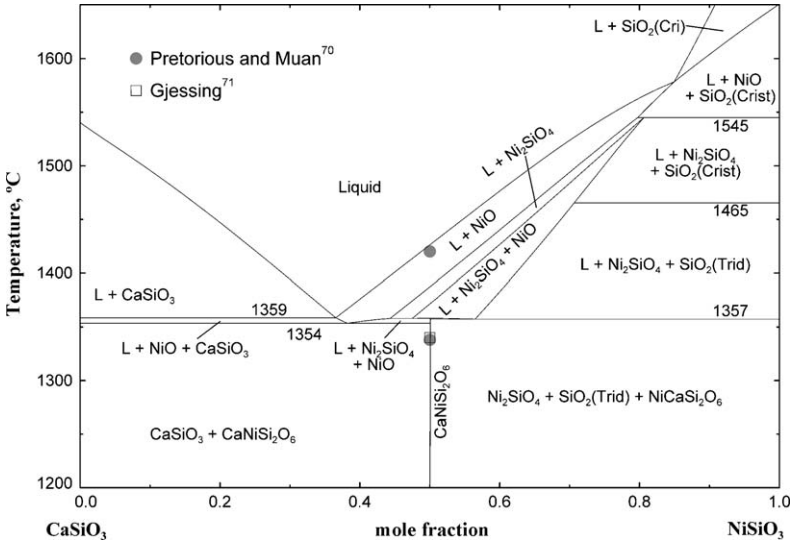

Fig. 8. Calculated phase diagram of the $CaSiO_3$–$NiSiO_3$ section along with experimental data.[70,71] Crist and Trid represent cristobalite (SiO_2) and tridymite (SiO_2), respectively.

first appearance temperature of liquid from the optical microscopic examination of quenched samples. The calculated solidus and liquidus temperatures are in agreement with the experimental results within 20 °C, as listed in Table 1.

Fig. 8 shows the calculated phase diagram of the $CaSiO_3$–$NiSiO_3$ section. Biggar[69] reported incongruent melting of $CaNiSi_2O_6$ at 1340 °C with a classical quenching technique followed by an optical microscopic phase determination. Pretorius and Muan[69,70] also reported the similar incongruent melting of $CaNiSi_2O_6$ at 1338 °C of and complete melting at 1420 °C. As shown in Fig. 8, the calculated solidus and liquidus temperatures of $CaNiSi_2O_6$ are in agreement with the experimental results. The primary crystalline phase at $CaNiSi_2O_6$ composition is calculated to be the NiO-rich monoxide phase.

The liquidus projection of the CaO–NiO–SiO_2 system is calculated in Fig. 9 using the optimized model parameters in this study. Very large NiO monoxide primary area can be calculated because the NiO–Ca_2SiO_4 is strong stable diagonal compared with CaO–Ni_2SiO_4 in the quadrilateral CaO–NiO–Ca_2SiO_4–Ni_2SiO_4.

The activities of solid NiO in liquid CaO–NiO–SiO_2 phase were determined at 1400 °C by Pretorius and Muan[74] from the equilibration of molten oxide, metallic Ni and CO_2/H_2 gas mixture. As shown in Fig. 10, the calculated results are in good agreement with experimental results. The iso-activity lines of NiO and SiO_2 at 1500 °C and 1600 °C are calculated in Fig. 11.

3.5. MgO–NiO–SiO_2 system

Mg_2SiO_4 and Ni_2SiO_4 can form a complete olivine solid solution. Rajamani et al.[75] observed that M1 sites were mainly occupied by Ni^{2+} (ionic radius = 0.069 nm) and M2 sites were mainly occupied by Mg^{2+} (ionic radius = 0.072 nm) from a single crystal X-ray diffraction analysis. After Rajamani et al., many investigations have been carried out to understand the olivine structure of the quenched samples using various techniques: single crystal X-ray,[76–79] powder X-ray diffraction,[80] crystal field spectroscopic,[81] EXAFS,[82] and neutron powder diffraction analysis.[82] The experimental results are summarized in Fig. 12. Chen et al.[80] mentioned that the true state of ordering in the olivine solutions at high temperatures might not be retained after quenching due to the rearrangement of cations during quenching process. Henderson et al.[82] investigated the temperature dependency of the ordering behaviour of $MgNiSiO_4$ olivine up to 1100 °C, using an *in situ* neutron powder diffraction technique. As shown in Fig. 13, the occupancy of Ni in M1 sites is decreasing toward 0.5 (random ordering) with increasing temperature at $T > 800$ °C. However, they found that the cation distribution does not reach an equilibrium state at

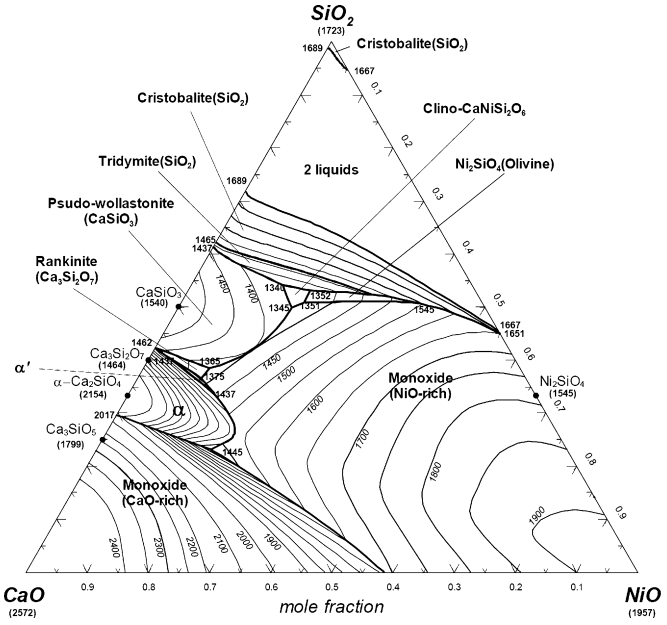

Fig. 9. Calculated liquidus projection of the NiO–CaO–SiO_2 system. Temperatures are in °C. α and α′ represent α-Ca_2SiO_4 and α′-Ca_2SiO_4, respectively.

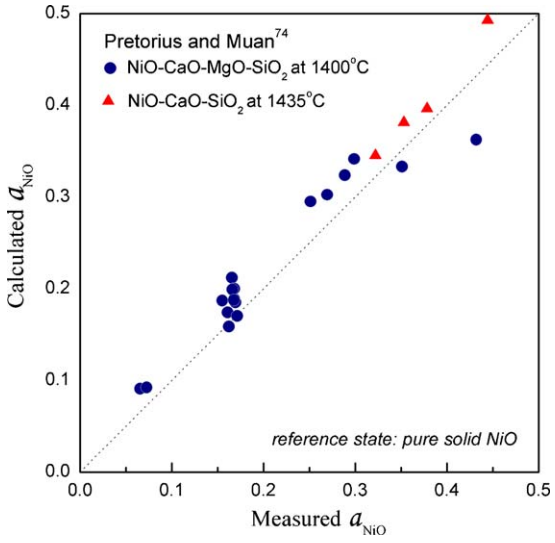

Fig. 10. The calculated and measured[74] activities of NiO in the NiO–CaO–SiO_2 system at 1435 °C and the NiO–CaO–MgO–SiO_2 system at 1400 °C (reference state is pure solid NiO).

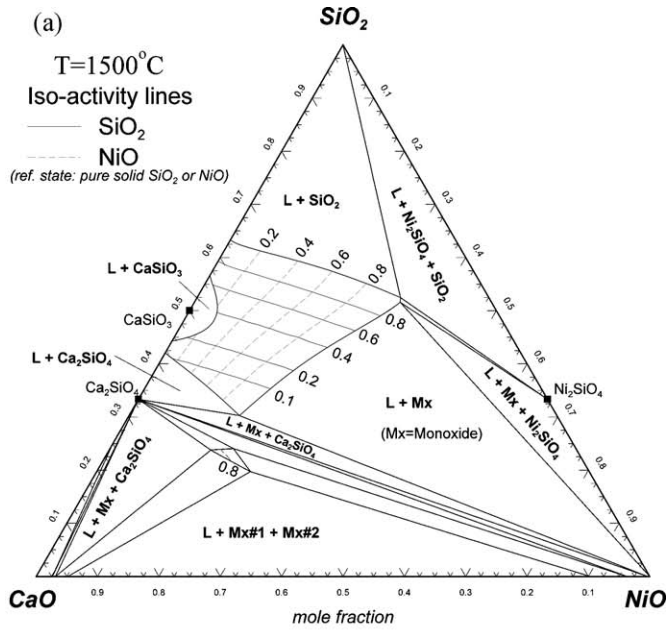

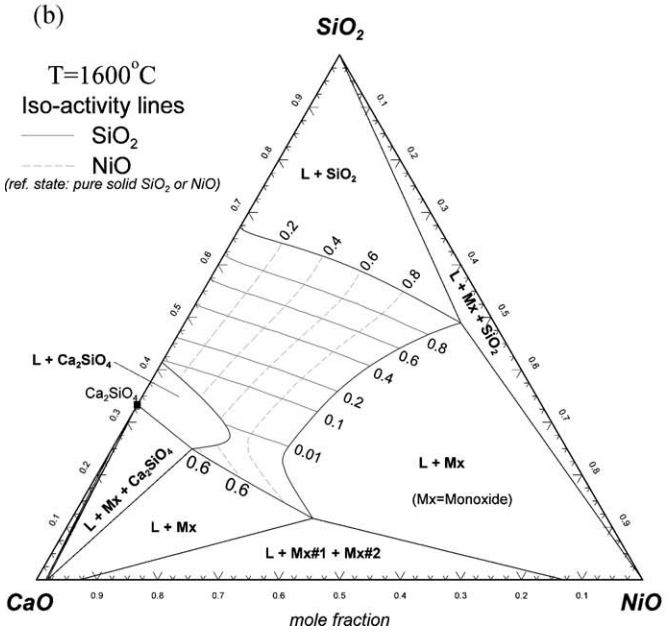

Fig. 11. Calculated iso-activity lines in the NiO–CaO–SiO_2 system at (a) 1500 °C and (b) 1600 °C (reference states are pure solid SiO_2(cristobalite) and pure solid NiO).

$T < 800$ °C; therefore only high temperature data can be used to optimize olivine model parameter to describe equilibrium ordering behaviour of the olivine solution.

Fig. 14 shows the oxygen partial pressures for the 'Mg_2SiO_4–Ni_2SiO_4 olivine solution + SiO_2 + metallic Ni' assemblage at various temperatures. Campbell and Roeder[48] measured the oxygen partial pressures using CO_2/H_2 gas mixtures at 1400 °C. Ottonello and Morlotti[83] and Boström and Rosén[84] used an EMF technique in the temperature range of 750–1200 °C and 972–1327 °C, respectively. The oxygen partial pressures are directly related to the activity of Ni_2SiO_4 of the olivine solution: $2Ni(s) + SiO_2(s) + O_2(g) = Ni_2SiO_4(olivine)$. The calculated oxygen partial pressures are in good agreement with the experimental data of Campbell and Roeder[48] and Boström and Rosén[84]. The experimental data of Ottonello and Morlotti[83] show inconsistency with the other data.

Mukhopadhyay and Jacob[64] and Seifert and O'Neill[85] investigated the phase equilibria (tie-line) between olivine and monoxide solutions at 1100 °C and at 973 °C, respectively, by employing an quenching technique followed by the EPMA or XRD phase analysis. As can be seen in Fig. 15, the experimental data of Seifert and O'Neill[85] were much scattered, as they mentioned the possibility of non-equilibration in their experiments. Thus, the experimental data of Mukhopadhyay and Jacob[64] were mainly considered in the present optimization. The calculated tie-lines are in good agreement with both experimental results within the experimental scatters.

The phase diagram of the Mg_2SiO_4–Ni_2SiO_4 orthosilicate section was investigated by Ringwood[37] using a classical quenching technique followed by an optical microscopic observation. As can be seen in Fig. 16, the calculated phase diagram of the Mg_2SiO_4–Ni_2SiO_4 section shows a rather large discrepancy with the experimental data of Ringwood[37]: the calculated solidus agrees with the experimental data within the experimental error limits, while the calculated liquidus is lower than the experimental data. However, as pointed out in the NiO–SiO_2 system, the decomposition temperature of Ni_2SiO_4 measured by Ringwood[37] is higher than other experimental results[38–40] by about 80 °C, which casts the doubt on his experimental accuracy. Ringwood[37] himself also mentioned a large uncertainty of temperature in his experiments.

After Dilaktovskii[86] observed the solubility of $NiSiO_3$ into $MgSiO_3$ (proto-enstatite), Campbell and Roeder[48] determined the solubility limit of $NiSiO_3$ in $MgSiO_3$ at 1400 °C more accurately by equilibrating 'pyroxene + olivine + SiO_2 + Ni' under CO_2/H_2 gas mixture. The oxygen partial pressure for the four phase equilibrium was determined to be $10^{-7.44}$ bar, which is calculated as $10^{-7.25}$ bar in the present study. Shirane[87]

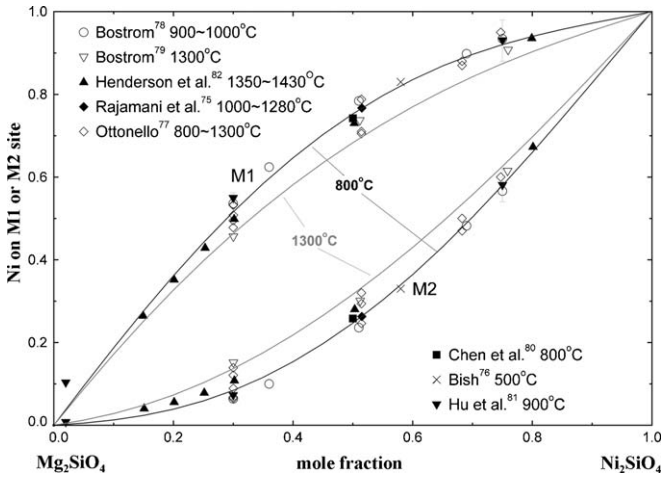

Fig. 12. Calculated cation distribution of Ni and Mg between M2 and M1 sites in olivine along with experimental data.[75–82]

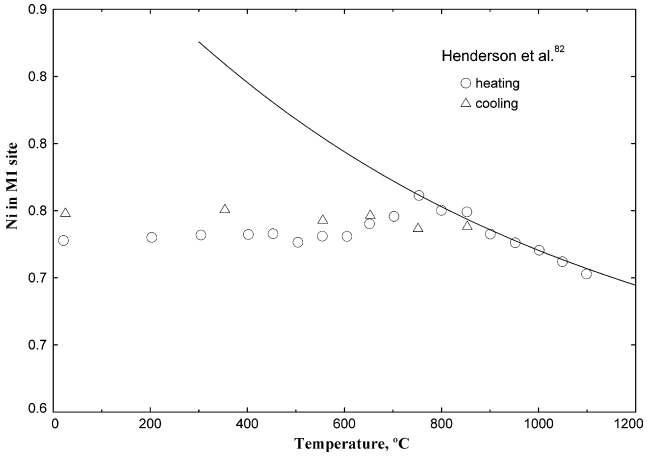

Fig. 13. Calculated Ni occupancy of M1 site in $MgNiSiO_4$ olivine with temperatures along with experimental data of Henderson et al.[82]

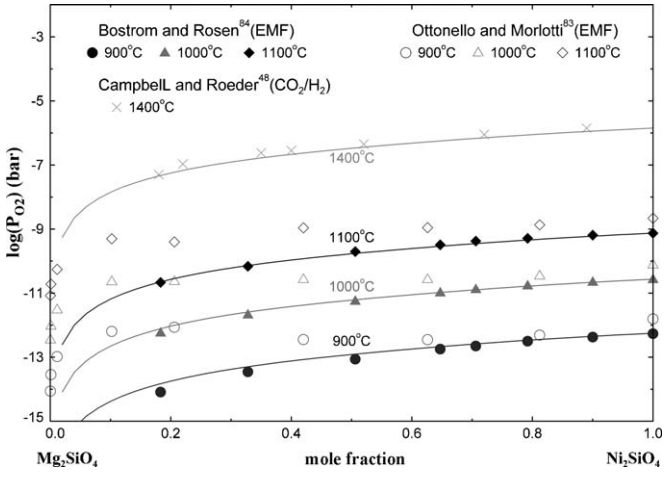

Fig. 14. Calculated equilibrium oxygen partial pressures for the olivine (Mg_2SiO_4–Ni_2SiO_4) + SiO_2 + Ni assemblage along with experimental data.[48,83,84]

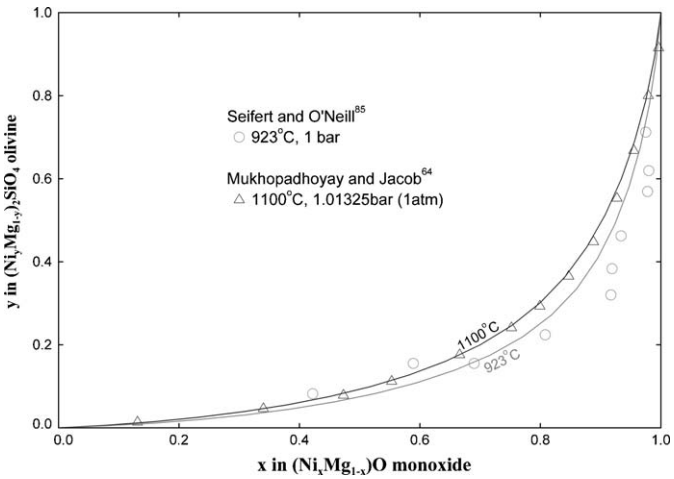

Fig. 15. Calculated phase relation between monoxide (MgO–NiO) and olivine (Mg_2SiO_4–Ni_2SiO_4) in comparison with experimental data.[64,85]

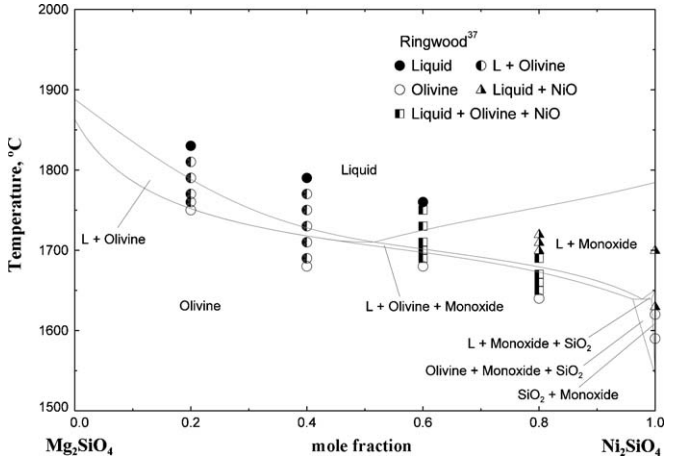

Fig. 16. Calculated phase diagram of the Mg_2SiO_4–Ni_2SiO_4 orthosilicate section with experimental data of Ringwood.[37]

investigated sub-solidus phase relations of the MgO–NiO–SiO_2 system at 1400 °C by means of XRD phase determination of the quenched samples. Pretorius and Muan[70] reported about 18 mol% solubility of $NiSiO_3$ into $MgSiO_3$ without any experimental details. The calculated phase diagram at 1400 °C is presented in Fig. 17 along with experimental data[48,87]. The maximum solubility of $NiSiO_3$ into $MgSiO_3$ measured by Campbell and Roeder[48] and Shirane[87] were 13 mol% and 12 mol%, respectively. The Gibbs energy of $NiSiO_3$ for the pyroxene solution was determined to reproduce the iso-thermal sections in Fig. 17. The calculated solubility of $NiSiO_3$ in $MgSiO_3$ at 1400 °C is 10.2 mol%, which is slightly lower than experimental data.

Grutzeck and Muan[40] determined the phase relations of the MgO–NiO–SiO_2 system using a classical quenching technique followed by the optical microscopy and XRD phase determinations. The primary crystalline phase boundary between SiO_2 and olivine was determined. The calculated liquidus projection in Fig. 18 is in agreement with experimental data[40]. Two invariant reactions, L → pyroxene + olivine + SiO_2 at 1547 °C and L → olivine + monoxide + SiO_2 at 1633 °C, were closely

Table 2
The invariant points measured by Grutzeck and Muan[40] in the NiO–MgO–SiO_2 system.

Invariant reaction		T (°C)	Liquid composition (mol%)			
			NiO	MgO	SiO_2	
L → olivine s.s. + pyroxene s.s + SiO_2(cristobalite)	Eutectic	1547	5.6	41.8	52.6	Exp.
		1530	6.0	42.7	51.3	Calc.
L → olivine s.s. + monoxide s.s + SiO_2(cristobalite)	Eutectic	1633	53.4	1.7	45.0	Exp.
L → olivine s.s. + monoxide s.s + SiO_2(cristobalite)		1639	53.3	1.8	44.9	Calc.
Temperature maximum on the olivine-silica boundary		1639	51.6	4.9	43.5	Exp.
		1643	46.4	7.6	46.0	Calc.

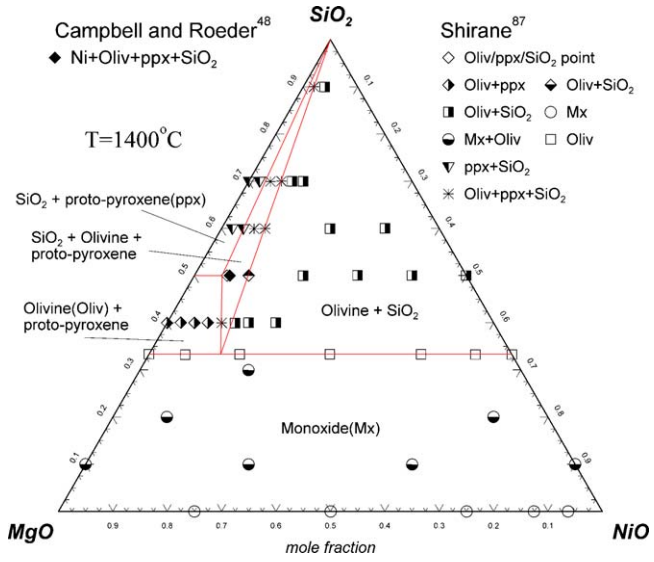

Fig. 17. Calculated phase diagram of the NiO–MgO–SiO_2 system at 1400 °C with experimental data.[48,87]

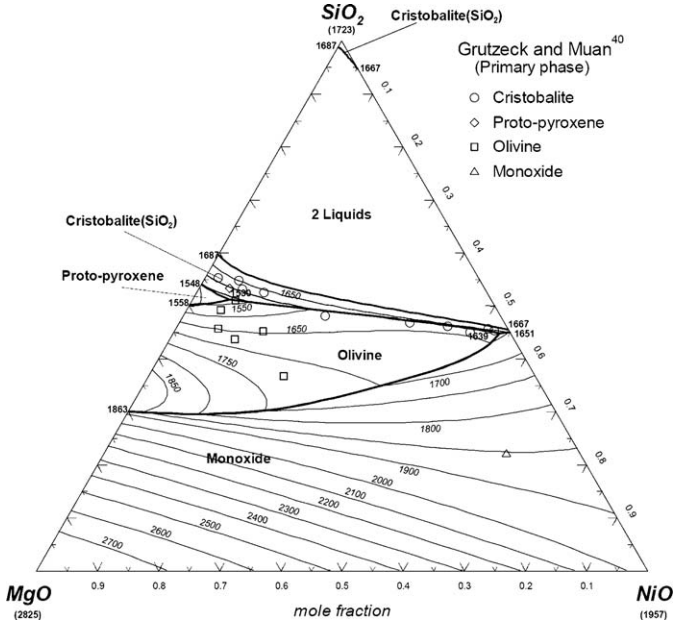

Fig. 18. Calculated liquidus projection of the MgO–NiO–SiO_2 system with experimentally determined primary phase by Grutzeck and Muan[40]. Temperatures are in °C.

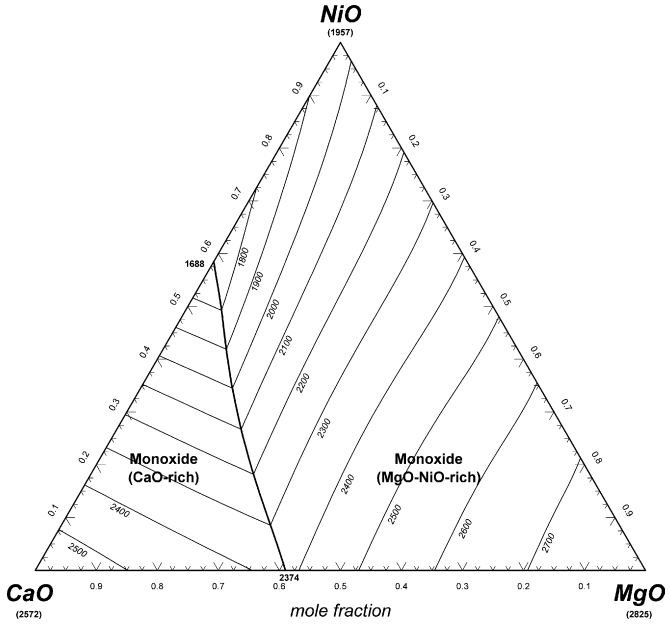

Fig. 19. Predicted liquidus projection of the CaO–MgO–NiO system in the present study. Temperatures are in °C.

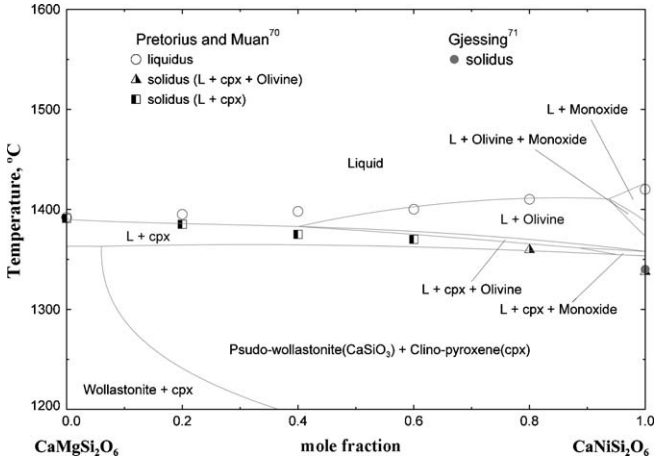

Fig. 20. Calculated phase diagram of the $CaMgSi_2O_6$–$CaNiSi_2O_6$ section along with experimental data.[70,71]

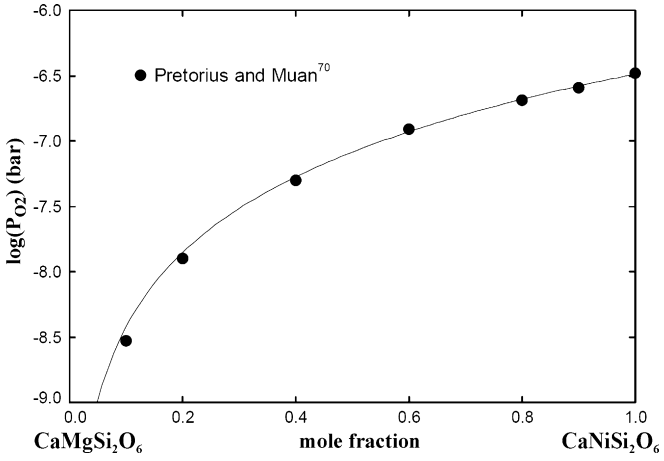

Fig. 21. Calculated equilibrium oxygen partial pressures for the clino-pyroxene ($CaMgSi_2O_6$–$CaNiSi_2O_6$) + $CaSiO_3$ + SiO_2 + Ni assemblage at 1350 °C in comparison with experimental data by Pretorius and Muan.[70]

reproduced in the present study, as listed in Table 2. The liquidus temperatures of several samples were observed by Grutzeck and Muan[40], which are also reasonably reproduced in the present study.

In order to reproduce the phase diagram in the MgO–NiO–SiO_2 system, one temperature dependent ternary parameter for liquid phase was introduced. The Mg_2SiO_4–Ni_2SiO_4 olivine solution was optimized using two-sublattice compound energy formalism based on the cation distribution data in Figs. 12 and 13 and phase equilibration data in Figs. 14 and 15. The Gibbs energies of two end-members, $(Mg)^{M2}[Mg]^{M1}SiO_4$ and $(Ni)^{M2}[Ni]^{M1}SiO_4$ are determined from their binary systems. The Gibbs energies of $(Mg)^{M2}[Ni]^{M1}SiO_4$ and $(Ni)^{M2}[Mg]^{M1}SiO_4$ were determined using $\Delta_{MgNi:NiMg}$ and I_{MgNi} model parameters to reproduce the experimental data. The reciprocal Gibbs energy change $\Delta_{MgNi:NiMg} = 0$ and the $I_{MgNi} = -16233.9$ J/mol were optimized. In addition, the interaction parameters between Ni and Mg in the M2 sublattice ($L_{Mg,Ni:Mg} = L_{Mg,Ni:Ni} = 11715.2$ J/mol) were required to reproduce the experimental data accurately.

3.6. CaO–MgO–NiO system

No phase diagram study for the CaO–MgO–NiO system has been conducted. The liquidus surface of the CaO–MgO–NiO system is predicted in Fig. 19 from the present model parameters. No ternary compounds were considered. As mentioned earlier, the thermodynamic properties of both liquid and monoxide were predicted using the 'Kohler-like'[20,21] interpolation technique without any additional ternary model parameters.

3.7. CaO–MgO–NiO–SiO_2 system

The experimental study on the phase diagram and thermodynamic properties for the quaternary CaO–MgO–NiO–SiO_2 system is very limited. Pretorius and Muan[70] mentioned the maximum solubilities of NiO in akermanite and monticellite phases were 4.46 and 20.17 mol%, respectively, at unspecified temperature. However, no experimental data were provided. The

Table 3
Optimized model parameters of the NiO–CaO–MgO–SiO_2 system (J/mol or J/(mol-K)).

Monoxide: $(Mg^{2+}, Ni^{2+}, Ca^{2+})O$
$q^{11}_{MgO,NiO} = -4393.2$, $q^{12}_{MgO,NiO} = 2928.8$
The model parameters of the CaO–NiO[27] and CaO–MgO[28] systems can be found in the previous studies.

Olivine: $(Mg^{2+}, Ni^{2+}, Ca^{2+})^{M2}(Mg^{2+}, Ni^{2+}, Ca^{2+})^{M1}SiO_4$
$G^o_{NiNi} = G^o(Ni_2SiO_4)$:
$\Delta H^o_{298\,K} = -1393930.0$
$S^o_{298\,K} = 128.1$ (from Robie[43])
$C_P = 215.0 - 1030.8T^{-0.5} - 4944530T^{-2} + 623705000T^{-3}$ (from Hirschimann[52])
$I_{CaNi} = G^o_{CaNi} - G^o_{NiCa} = 0$
$\Delta_{CaNi:NiCa} = G^o_{CaCa} + G^o_{NiNi} - G^o_{CaNi} - G^o_{NiCa} = -83680$
$I_{MgNi} = G^o_{MgNi} - G^o_{NiMg} = -16233.9$
$\Delta_{MgNi:NiMg} = G^o_{MgMg} + G^o_{NiNi} - G^o_{MgNi} - G^o_{NiMg} = 0$
${}^0L_{Mg,Ni:Mg} = {}^0L_{Mg,Ni:Ni} = 11715.2$
The model parameters of the CaO–MgO–SiO_2 system can be found in the previous study.[5]

Proto-pyroxene: $(Ca^{2+}, Mg^{2+}, Ni^{2+})^{M2}(Mg^{2+}, Ni^{2+})^{M1}Si_2O_6$
$G^o_{NiNi} = 2G^o(NiSiO_3, proto-)$
$G^o(NiSiO_3, proto-) = G^o(NiO(s)) + G^o(SiO_2(tridymite)) - 114.6 + 11.9T$
$I_{MgNi} = G^o_{MgNi} - G^o_{NiMg} = 0$
$\Delta_{MgNi:NiMg} = G^o_{MgMg} + G^o_{NiNi} - G^o_{MgNi} - G^o_{NiMg} = 0$
[a] $G^o_{CaNi} = G^o(CaNiSi_2O_6, proto-) = G^o(CaNiSi_2O_6, clino-) + 17071.2$
[b] ${}^0L_{Ca,Mg:Ni} = 25304.0 + 2.358T$
The model parameters of the CaO–MgO–SiO_2 system can be found in the previous study.[5]

Clino-pyroxene ($CaMgSi_2O_6$–$CaNiSi_2O_6$): $(Ca^{2+}, Mg^{2+}, Ni^{2+})^{M2}(Mg^{2+}, Ni^{2+})^{M1}Si_2O_6$
$G^o_{NiNi} = 2G^o(NiSiO_3, clino-)$
$G^o(NiSiO_3, clino-) = G^o(NiO(s)) + G^o(SiO_2(tridymite)) + 41840.0$
$G^o_{CaNi} = G^o(CaNiSi_2O_6, clino-)$:
$\Delta H^o_{298\,K} = -2792500.0$
$S^o_{298\,K} = S^o_{298\,K}(CaO(s)) + S^o_{298\,K}(NiO(s)) + S^o_{298\,K}(SiO_2(tridymite)) - 8.2 = 162.0$
$C_P = C_P(CaO(s)) + C_P(NiO(s)) + C_P(SiO_2(tridymite))$
$I_{MgNi} = G^o_{MgNi} - G^o_{NiMg} = 0$
$\Delta_{MgNi:NiMg} = G^o_{MgMg} + G^o_{NiNi} - G^o_{MgNi} - G^o_{NiMg} = 0$
[c] ${}^0L_{Ca,Mg:Ni} = 25304.0 + 2.358T$, ${}^1L_{Ca,Mg:Ni} = -3018.6$
The model parameters of the CaO–MgO–SiO_2 system can be found in the previous study.[5]

Liquid oxide
NiO–SiO_2 binary parameters:
$q^{00}_{NiSi} = -2301.2 + 14.2T$, $q^{01}_{NiSi} = 12552.0$, $q^{07}_{NiSi} = 725924.0 - 251.0T$
NiO–MgO binary parameters:
$q^{00}_{NiMg} = -8368.0$
Ternary parameters
$q^{001}_{CaSi(Ni)} = 107131.3 - 72.5T$, $q^{001}_{NiSi(Ca)} = -12552.0$
$q^{001}_{NiSi(Mg)} = -50208.0$, $q^{001}_{MgSi(Ni)} = 8368.0$
$Z_{CaCa} = Z_{NiNi} = 1.3774$, $Z_{SiSi} = 2.7548$.
The other binary model parameters for the liquid oxide can be found in the previous studies[28,32,33].

The Gibbs energies of end-member of the solid and liquid solutions and of the other stoichiometric compounds are taken from the F*A*C*T database[29,30] and previous study.[5]

[a] The value is identical to the Gibbs energy of proto-$CaMgSi_2O_6$ = clino-$CaMgSi_2O_6$ + 4080.1 obtained in previous study.[5]

[b] The value is identical to ${}^0L_{Ca,Mg:Mg}$ obtained in previous study.[5]

[c] The values are identical to ${}^0L_{Ca,Mg:Mg}$ and ${}^1L_{Ca,Mg:Mg}$ obtained in previous study.[5]

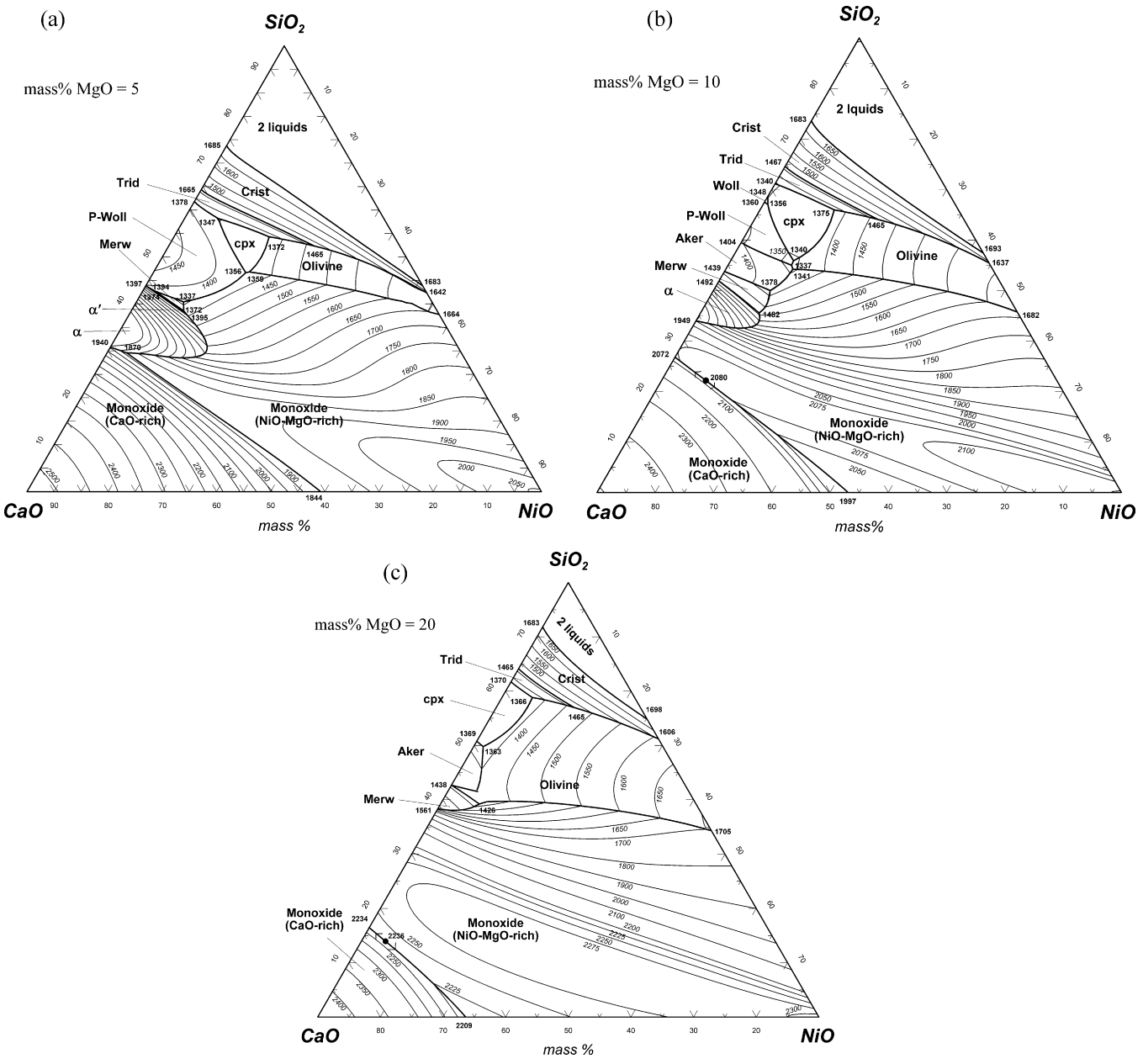

Fig. 22. Predicted liquidus projections of the NiO–CaO–MgO–SiO_2 system at constant MgO contents: (a) mass % MgO = 5, (b) mass % MgO = 10 and (c) mass % MgO = 20. Temperatures are in °C. Legends: cpx, clino-pyroxene; Woll, wollastonite ($CaSiO_3$); P-Woll, pseudowollastonite ($CaSiO_3$); Crist, cristobalite (SiO_2); Tid, tridymite (SiO_2); α, α-Ca_2SiO_4; α′, α′-Ca_2SiO_4; Merw, $MgCa_3Si_2O_8$; Aker, $MgCa_2Si_2O_7$.

clino-pyroxene $CaMgSi_2O_6$–$CaNiSi_2O_6$ solution is found in the system.

White et al.[88] reported a complete clino-pyroxene solid solution between $CaMgSi_2O_6$ (diopside) and $CaNiSi_2O_6$ (niopside) from the XRD analysis for the annealed/quenched samples. Wright and Navrotsky[89] determined the enthalpy of mixing of $CaNi_{0.5}Mg_{0.5}Si_2O_6$ from solid $CaMgSi_2O_6$ and $CaNiSi_2O_6$ using a $2PbO{\cdot}B_2O_3$ solution calorimeter. The measured enthalpy of mixing was -3.04 ± 0.71 kJ/mol at 702 °C. Pretorius and Muan[70] measured the equilibrium oxygen partial pressures for the $CaMgSi_2O_6$–$CaNiSi_2O_6$ clino-pyroxene + $CaSiO_3$ + SiO_2 + metallic Ni assemblage using CO_2/H_2 gas mixture at 1350 °C and determined the solidus and liquidus of the $CaMgSi_2O_6$–$CaNiSi_2O_6$ clino-pyroxene section using a classical quenching technique followed by an optical microscopic phase determination. The experimental data of Pretorius and Muan[70] are compared with the present calculations in Figs. 20 and 21. The calculated oxygen partial pressures are in good agreement with experimental data, and the solidus and liquidus of the clino-pyroxene agree with experimental data within 25 °C.

It was found that these experimental data can be reproduced with assumption that $CaNiSi_2O_6$ and $CaMgSi_2O_6$ forms an ideal solution. Although the experimental data of Wright and Navrotsky[89] can be reproduced with negative interaction parameter between Mg and Ni in the M1 site,

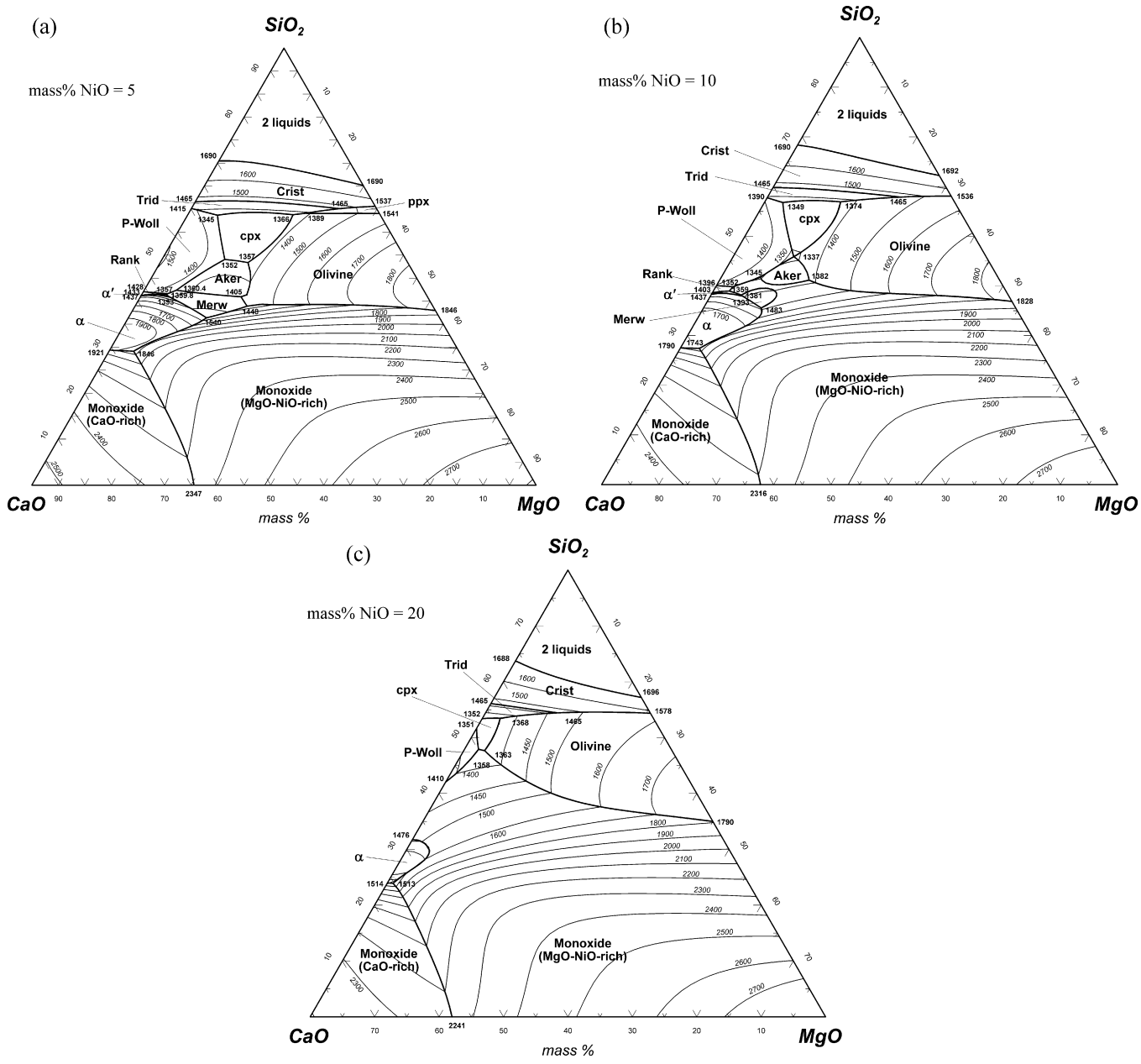

Fig. 23. Predicted liquidus projection of the NiO–CaO–MgO–SiO_2 system at constant NiO contents: (a) mass % NiO = 5, (b) mass % NiO = 10, (c) mass % NiO = 20. Temperatures are in °C. Legends: cpx, clino-pyroxene; P-Woll, pseudowollastonite ($CaSiO_3$); Crist, cristobalite (SiO_2); Trid, tridymite (SiO_2); α, α-Ca_2SiO_4; α′, α′-Ca_2SiO_4; Merw, $Ca_3MgSi_2O_8$; Aker, $Ca_2MgSi_2O_7$; Rank, $Ca_3Si_2O_7$; ppx, Proto-pyroxene.

$L_{Ca:Mg,Ni}$, this can noticeably increase the liquidus of clino-pyroxene in Fig. 20 and reduce the oxygen partial pressures in Fig. 21. That is, the experimental results of Wright and Navrotsky[89] are slightly inconsistent with experimental data by Pretorius and Muan[70]. In the present study, the experimental data by Pretorius and Muan[70] were considered more accurately. Among 6 end-members of clino-pyroxene solution, $(Ca,Mg,Ni)^{M2}[Mg,Ni]^{M1}Si_2O_6$, the Gibbs energies of $CaMgSi_2O_6$ and $Mg_2Si_2O_6$ were determined in the previous study[5] for the modeling of the CaO–MgO–SiO_2 system and the Gibbs energy of $CaNiSi_2O_6$ was determined in the present study for the CaO–NiO–SiO_2 system. The Gibbs energy of $Ni_2Si_2O_6$ was adjusted to minimize the solubility of $Ni_2Si_2O_6$ into $CaNiSi_2O_6$. The Gibbs energy of the imaginary $MgNiSi_2O_6$ and $NiMgSi_2O_6$ end-members were fixed with assumption that reciprocal Gibbs energy change $\Delta_{MgNi:NiMg} = 0$ and the inverse energy $I_{MgNi} = 0$.

The activities of NiO in liquid CaO–MgO–NiO–SiO_2 slag at 1400 °C were determined by Pretorius and Muan[74] from the equilibration of molten oxide, metallic Ni and CO_2/H_2 gas mixture. As shown in Fig. 10, the calculated activities of NiO agree well with experimental data[74].

Using the present optimized model parameters in Table 3, the unexplored phase diagrams of the quaternary CaO–MgO–NiO–SiO_2 system were calculated and the results are presented in Figs. 22 and 23. In the present study,

$Ca_2MgSi_2O_7$ (akermanite) was treated as a stoichiometric compound. Since monticellite ($CaMgSiO_4$) is part of the olivine solution, the solubility of Ni into monticellite phase was counted in the modeling of olivine solution. The liquidus projections of the CaO–NiO–SiO_2 system with the addition of 5, 10 and 20 wt% MgO are predicted in Fig. 22. As can be seen in the figure, the primary crystalline area of olivine is rapidly enlarged with increasing MgO. The liquidus projections of the CaO–MgO–SiO_2 with the addition of 5, 10 and 20 wt% NiO are predicted in Fig. 23. The monoxide crystalline area is enlarged with increasing NiO content.

4. Summary

A complete critical evaluation of all available phase diagrams, thermodynamic and structural data for the CaO–MgO–NiO–SiO_2 system at a total pressure of 1 bar has been made, and parameters of thermodynamic models have been optimized to reproduce all reliable experimental data within experimental error limits. The phase diagrams for the CaO–NiO–SiO_2, MgO–NiO–SiO_2, and CaO–MgO–NiO systems were calculated using the optimized model parameters. In particular, as results of the present thermodynamic modeling, the unexplored phase diagrams for the CaO–MgO–NiO–SiO_2 quaternary system were predicted for the first time. The database of the model parameters can be used along with software for Gibbs energy minimization in order to calculate all thermodynamic properties and any phase diagram section or phase equilibrium of interest.

Acknowledgements

This project was partially supported by the NSERC, Canada. One of the authors, D.-H. Woo, would like to thank to POSCO for financial support for the visit to McGill University to carry out this research.

References

1. Grimsey EJ, Biswas AK. Solubility of nickel in silica-saturated iron silicate slags at 1573 K. *Inst Min Metall Trans C* 1976;**85**:200–7.
2. Burkun A. *Extractive metallurgy of nickel*. New York: John Wiley and Sons; 1985.
3. Wood B, Banno S. Garnet–orthopyroxene and orthopyroxene–clinopyroxene relationships in simple and complex systems. *Contrib Miner Petrol* 1973;**42**(2):109–24.
4. Berger E, Vannier M. Les dunites en enclaves dans les basaltes alcalins des les oc aniques: approche p trologique. *Bulletin de min ralogie* 1984;**107**(5):649–63.
5. Jung I-H, Decterov S, Pelton AD. Critical thermodynamic evaluation and optimization of the CaO–MgO–SiO_2 system. *J Eur Ceram Soc* 2005;**25**(4):313–33.
6. Jung I-H, Decterov S, Pelton AD. Critical thermodynamic evaluation and optimization of the MgO–Al_2O_3, CaO–MgO–Al_2O_3, and MgO–Al_2O_3–SiO_2 systems. *J Phase Equilibr* 2004;**25**(4):329–45.
7. Jung I-H, Decterov S, Pelton AD. Critical thermodynamic evaluation and optimization of the FeO–Fe_2O_3–MgO–SiO_2 system. *Metall Mater Trans B* 2004;**35**(5):877–89.
8. Jung I-H, Decterov S, Pelton AD. Critical thermodynamic evaluation and optimization of the Fe–Mg–O system. *J Phys Chem Solids* 2004;**65**(10):1683–95.
9. Jung I-H, Decterov S, Pelton AD. Thermodynamic modeling of the Co–Fe–Si–O system. *Int J Mater Res* 2007;**98**:816–25.
10. Pelton AD, Blander M. Thermodynamic analysis of ordered liquid solutions by a modified quasichemical approach—application to silicate slags. *Metall Mater Trans B* 1986;**17**(4):805–15.
11. Pelton AD, Blander M. Computer-assisted analysis of the thermodynamic properties and phase diagrams of slags. In: *Proceedings of the second international symposium on metallurgical slags and fluxes*. Warrendale, PA: TMS-AIME, 1984. p. 281–94.
12. Jung I-H, Decterov S, Pelton AD. Thermodynamic modeling of the MgO–Al_2O_3–CrO–Cr_2O_3 system. *J Am Ceram Soc* 2005;**88**(7):1921–8.
13. Jung I-H. Critical evaluation and thermodynamic modeling of the Mn–Cr–O system for the oxidation of SOFC interconnect. *Solid State Ionics* 2006;**177**(7–8):765–77.
14. Jung I-H, Kang Y-B, Decterov S, Pelton AD. Thermodynamic evaluation and optimization of the MnO–Al_2O_3 and MnO–Al_2O_3–SiO_2 systems and applications to inclusion engineering. *Metall Mater Trans B* 2004;**35**(2):259–68.
15. Kang Y-B, Jung I-H, Decterov SA, Pelton AD, Lee H-G. Critical thermodynamic evaluation and optimization of the CaO–MnO–SiO_2 and CaO–MnO–Al_2O_3 systems. *ISIJ Int* 2004;**44**(6):965–74.
16. Kang Y-B, Jung I-H, Decterov SA, Pelton AD, Lee H-G. Phase equilibria and thermodynamic properties of the CaO–MnO–Al_2O_3–SiO_2 system by critical evaluation, modeling and experiment. *ISIJ Int* 2004;**44**(6):975–83.
17. Kang Y-B, Jung I -H, Lee H -G. Critical thermodynamic evaluation and optimization of the MnO–SiO_2–TiO_2–Ti_2O_3 system. *Calphad* 2006;**30**(3):226–34.
18. Kang Y-B, Jung I-H, Lee H-G. Critical thermodynamic evaluation and optimization of the MnO–TiO_2–Ti_2O_3 system. *Calphad* 2006;**30**(3):235– 47.
19. Arnout S, Guo M, Jung I-H, Blanpain B, Wollants P. Experimental determination of CaO–CrO–Cr_2O_3–MgO–SiO_2 and thermodynamic modeling of the CrO–Cr_2O_3–MgO–SiO_2 system. *J Am Ceram Soc* 2009;**92**(8):1831–9.
20. Pelton AD. A general "geometric" thermodynamic model for multicomponent solutions. *Calphad* 2001;**25**(2):319–28.
21. Chartrand P, Pelton AD. On the choice of "Geometric" thermodynamic models. *J Phase Equilib* 2000;**21**(2):141–7.
22. Deer WA, Howie RA, Zussman J. *An introduction to the rock-forming minerals*. Hong Kong: Longman House; 1966.
23. Lumpkin GR, Ribbe PH. Composition, order-disorder and lattice parameters of olivines: relationships in silicate, germanate, beryllate, phosphate and borate olivines. *Am Miner* 1983;**68**(1–2):164–76.
24. Lumpkin GR, Ribbe PH, Lumpkin NE. Composition, order-disorder and lattice parameters of olivines: determinative methods for Mg–Mn and Mg–Ca silicate olivines. *Am Miner* 1983;**68**(11–12):1174–82.
25. Shannon RD. Revised effective ionic radii and systematic studies of interatomic distances in halides and chalcogenides. *Acta Crystallogr* 1976;**32**:751–67.
26. Hillert M, Jansson B, Sundman B. Application of the compound-energy model to oxide systems. *Z Metallkd* 1988;**79**(2):81–7.
27. Pelton AD. Thermodynamically optimised phase diagrams of oxide systems. In: *CRCT, Ecole Polytechnique de Montreal, Final report for phase diagram for ceramist*. 1994.
28. Wu P, Eriksson G, Pelton AD. Critical evaluation and optimization of the thermodynamic properties and phase diagrams of the CaO–FeO, CaO–MgO, CaO–MnO, FeO–MgO, FeO–MnO, and MgO–MnO Systems. *J Am Ceram Soc* 1993;**76**(8):2065–75.
29. Bale CW, Belisle E, Chartrand P, Decterov SA, Eriksson G, Hack K, et al. FactSage thermochemical software and databases—recent developments. *Calphad* 2009;**33**(2):295–311.
30. Bale CW, Chartrand P, Degterov SA, Eriksson G, Hack K, Ben Mahfoud R, et al. FactSage thermochemical software and databases. *Calphad* 2002;**26**(2):189–228.

31. Berman RG. Internally-consistent thermodynamic data for minerals in the system. *J Petrol* 1988;**29**:445–522.
32. Eriksson G, Wu P, Blander M, Pelton AD. Critical evaluation and optimization of the thermodynamic properties and phase diagrams of the MnO–SiO_2 and CaO–SiO_2 systems. *Can Metall Q* 1994;**33**(1):13–21.
33. Wu P, Eriksson G, Pelton AD, Blander M. Prediction of the thermodynamic properties and phase diagrams of silicate systems—evaluation of the FeO–MgO–SiO_2 system. *ISIJ Int* 1993;**33**(1):26.
34. Alejandro Cruz R, Antonio Romero S, Marissa Vargas R, Manuel Hallen L. Thermodynamic analysis of the SiO_2–NiO–FeO system. *J Non-Cryst Solids* 2005;**351**(16–17):1359–65.
35. Greig JW. Immiscibility in silicate melts. *Am J Sci* 1927;**13**(74):133–54.
36. Babayan SA. Stable liquidation in FeO–SiO_2, CoO–SiO_2, and NiO–SiO_2. *Armyanskii Khimicheskii Zhurnal* 1975;**28**(7):533–9.
37. Ringwood AE. Melting relationships of Ni–Mg olivines and some geochemical implications. *Geochim Cosmochim Acta* 1956;**10**:297–303.
38. Phillips B, Hutta JJ, Warshaw I. Phase equilibria in the system NiO–Al_2O_3–SiO_2. *J Am Ceram Soc* 1963;**46**(12):579–83.
39. O'Neill HSC. Free energies of formation of NiO, CoO, Ni_2SiO_4, and Co_2SiO_4. *Am Miner* 1987;**72**(3–4):280–91.
40. Grutzeck MW, Muan A. Phase relations at liquidus temperatures in the system MgO–NiO–SiO_2. *J Am Ceram Soc* 1988;**71**(8):638–43.
41. Grutzeck MW, Muan A. Phase relations in the system iron oxide–NiO–SiO_2 under strongly reducing conditions. *J Am Ceram Soc* 1992;**75**(6):1351–6.
42. Watanabe H. Thermochemical properties of synthetic high-pressure compounds relevant to the earth's mantle. *High Pressure Res* 1982: 441–64.
43. Robie RA, Hemingway BS, Ito J, Krupka KM. Heat capacity and entropy of Ni_2SiO_4–olivine from 5 to 1000 K and heat capacity of Co_2SiO_4 from 360 to 1000 K. *Am Miner* 1984;**69**(11–12):1096–101.
44. Navrotsky A. Ni_2SiO_4-enthalphy of the olivine–spinel transition by solution calorimetry at 713 °C. *Earth Planet Sci Lett* 1973;**19**(4):471–5.
45. Sugawara T, Akaogi M. Calorimetric measurements of fusion enthalpies for Ni_2SiO_4 and Co_2SiO_4 olivines and application to olivine-liquid partitioning. *Geochim Cosmochim Acta* 2003;**67**(14):2683–93.
46. Lebedev BG, Levitskii VA. The nickel orthosilicate–carbon monoxide equilibrium at high temperatures. *Russ J Phys Chem* 1961;**35**:1380–2.
47. Burdese A, Abbattista F, Damiani R. Equilibri di riduzione de silicati di ferro cobolto e nichel. *Metallurgii Italiane* 1963;**55**:557–9.
48. Campbell FE, Roeder P. The stability of olivine and pyroxene in the Ni–Mg–Si–O system. *Am Miner* 1968;**53**:257–68.
49. Rog G, Borchardt G. Thermodynamics of nickel orthosilicate. *J Chem Thermodyn* 1984;**16**(12):1103–5.
50. Levitskii VA, Golavanova YG, Popov SG, Chentsov VN. Thermodynamics of binary oxide systems: thermodynamic properties of Ni orthosilicate. *Russ J Phys Chem* 1975;**49**:971.
51. Taylor RW, Schmalzried H. The free energy of formation of some titanates, silicates, and magnesium aluminate from measurements made with galvanic cells involving solid electrolytes. *J Phys Chem* 1964;**68**(9):2444–9.
52. Hirschmann M. Thermodynamics of multicomponent olivines and the solution properties of $(Ni,Mg,Fe)_2SiO_4$ and $(Ca,Mg,Fe)_2SiO_4$ olivines. *Am Miner* 1991;**76**(7–8):1232–48.
53. Wartenberg HV, Prophet E. Melting diagrams of refractory oxides. V: Systems with MgO. *Z Anorg Allg Chem* 1932;**208**:369–79.
54. Nussler HB, Kubaschewski O. Thermochemistry of the system MgO–NiO. *Z Phys Chem* 1980;**127**:187–91.
55. Jakobsson A, Sichen D, Seetharama S. Thermodynamic study of the NiO–MgO system in the temperature range 1073 to 1473 K by a galvanic cell technique. *Metall Mater Trans B* 1993;**24**(6):1023–30.
56. Zinkevich M, Geupel S, Aldinger F. Thermodynamic assessment of the ternary systems Ga–Mg–O, Ga–Ni–O, Mg–Ni–O and extrapolation to the Ga–Mg–Ni–O phase diagram. *J Alloys Compd* 2005;**393**(1–2): 154–66.
57. Davies PK, Navrotsky A. Thermodynamics of solid solution formation in NiO–MgO and NiO–ZnO. *J Solid State Chem* 1981;**38**(2):264–76.
58. Ariya SM, Borisova NV, Morozova MP. Measurements of the activity NiO in solid NiO–MgO solutions at 900 and 1000 °C. *Russ J Phys Chem* 1972;**6**:123–4.
59. Evans LG, Muan A. Activity–composition relations of solid solutions and stabilities of end-member compounds in the system MgO–NiO–TiO_2 in contact with metallic nickel at 1400 °C. *Thermochim Acta* 1971;**2**(2):121–34.
60. Hahn Jr WC, Muan A. Activity measurements in oxide solid solutions: the systems NiO–MgO and NiO–MnO in the temperature interval 1100–1300 °C. *J Phys Chem Solids* 1961;**19**(3/4):338–48.
61. Seetharaman S, Abraham KP. Thermodynamic activities of NiO in NiO–MgO solid solutions. *Indian J Technol* 1968;**6**(4):123–4.
62. Kale GM. Activity–composition relations in the NiO–MgO system at 1300 K by the solid-state galvanic cell technique. *J Am Ceram Soc* 1991;**74**(9):2209–13.
63. Kreidler ER, Park HD. Activity of NiO in (Ni,Mg)O solid solutions. *J Am Ceram Soc* 1994;**77**(9):2491–3.
64. Mukhopadhyay S, Jacob KT. Tie lines and activities in the system NiO–MgO–SiO_2 at 1373 K. *J Phase Equilib* 1995;**16**(3):243–53.
65. Shirane Y, Nabika S, Sakamoto S, Nakashima I. Activity measurements in the oxide solid solutions of NiO–MgO and NiO–MgO–SiO_2 systems in the temperature range between 1073 and 1273 K. *Int J Miner Process* 1987;**19**(1–4):237–51.
66. Petot C, Petot-Ervas G, Rigaud M. Study of the thermodynamic properties of the solid solutions of magnesium and nickel oxides. *Can Metall Q* 1971;**10**(3):203–5.
67. Shannon RD, Vincent H. Relationships between covalency, interatomic distances and magnetic properties in halides and chalcogenides. *Struct Bond* 1974;**19**:1–43.
68. Propach V, Reinen D, Drenkhahn H, Miiller-Buschbaum H. Uber die Farbe von NiO. *Z Naturforsch* 1978;**33**:619–21.
69. Biggar GM. The system CaO–NiO–SiO_2. *J Am Ceram Soc* 1969;**52**(6):316–7.
70. Pretorius EB, Muan A. Stability of $CaNiSi_2O_6$("Niopside") and activity–composition relations of $CaMgSi_2O_6$–$CaNiSi_2O_6$ solid solutions at 1350 °C. *J Am Ceram Soc* 1992;**75**(6):1458–62.
71. Gjessing L. Contribution a L'étude des métasilicates. *Nor Geol Tidsskr* 1941;**20**:265–7.
72. Mukhopadhyay S, Jacob KT. Phase equilibria in the system NiO–CaO–SiO_2 and Gibbs energy of formation of $CaNiSi_2O_6$. *Metall Mater Trans A* 1995;**26A**(9):2311–5.
73. Navrotsky A, Coons WE. Thermochemistry of some pyroxenes and related compounds. *Geochim Cosmochim Acta* 1976;**40**(10):1281–8.
74. Pretorius EB, Muan A. Activity of nickel(II) oxide in silicate melts. *J Am Ceram Soc* 1992;**75**(6):1490–6.
75. Rajamani V, Brown GE, Prewitt CT. Cation ordering in Ni–Mg olivine. *Am Miner* 1975;**60**:292–9.
76. Bish D. Cation ordering in synthetic and natural Ni–Mg olivine. *Am Miner* 1981;**66**(7–8):770–6.
77. Ottonello G, Della Giusta A, Molin G. Cation ordering in Ni–Mg olivines. *Am Miner* 1989;**74**(3–4):411–21.
78. Boström D. Single-crystal X-ray diffraction studies of synthetic Ni–Mg olivine solid solutions. *Am Miner* 1987;**72**:965–72.
79. Boström D. Cation ordering at 1300 °C in the (Ni,Mg)–olivine solid solution series. *Acta Chem Scand* 1989;**43**:116–20.
80. Chen J, Li R, Parise J, Weidner D. Pressure-induced ordering in $(Ni,Mg)_2SiO_4$ olivine. *Am Miner* 1996;**81**:1519–22.
81. Hu X, Langer K, Boström D. Polarized electronic absorption spectra and Ni–Mg partitioning in olivines $(Mg_{1-x}Ni_x)_2SiO_4$. *Eur J Miner* 1990;**2**(1):29.
82. Henderson C, Redfern S, Smith R, Knight K, Charnock J. Composition and temperature dependence of cation ordering in Ni–Mg olivine solid solutions: a time-of-flight neutron powder diffraction and EXAFS study. *Am Miner* 2001;**86**(10):1170–87.
83. Ottonello G, Morlotti R. Thermodynamics of the (nickel + magnesium) olivine solid solution. *J Chem Thermodyn* 1987;**19**(8):809–18.
84. Boström D, Rosén E. Determination of activity–composition relations in $(Ni, Mg)_2SiO_4$ solid solutions at 1200–1600 K by solid-state EMF measurements. *Acta Chem Scand* 1988;**42**(3):149–55.
85. Seifert S, O'Neill HSC. Experimental determination of activity–composition relations in Ni_2SiO_4–Mg_2SiO_4 and

Co_2SiO_4–Mg_2SiO_4 olivine solid solutions at 1200 K and 0.1 MPa and 1573 K and 0.5 GPa. *Geochim Cosmochim Acta* 1987;**51**(1):97–104.
86. Dilaktovskii NL. Solubility of NiO in silicates. *Khim Referat Zhur* 1941;**4**(2):26.
87. Shirane Y. Phase relations in the NiO–MgO–SiO_2 systems at 1400 °C. *J Japan Inst Met* 1975;**39**(9):908–16.
88. White WB, McCarthy GJ, Scheetz BE. Optical spectra of chromium, nickel, and cobalt-containing pyroxenes. *Am Miner* 1971;**56**(72):79.
89. Wright DP, Navrotsky A. A thermochemical study of the distribution of cobalt and nickel between diopsidic pyroxene and melt. *Geochim Cosmochim Acta* 1985;**49**(11):2385–93.